

Wave Normal Direction and Spectral Properties of Whistler Mode Hiss Observed on the DE 1 Satellite

VIKAS S. SONWALKAR AND UMRAN S. INAN

STAR Laboratory, Stanford University, Stanford, California

A new study of magnetospheric hiss as a spatially and temporally enduring phenomenon is undertaken using a recently developed formalism that allows the representation of hiss by a field distribution function (FDF). This formalism explicitly takes into account the whistler mode relationships and the linear and spin motion of the satellite, so that on a spin-stabilized satellite, it becomes possible to measure the wave propagation direction(s) from the observed fading patterns in the received electromagnetic field data. We have analyzed hiss signals received by electric and magnetic field antennae aboard the DE 1 satellite during a ~ 3 -hour period on September 23, 1983. A band of hiss at frequencies < 2 kHz was observed continuously from 0236 UT to 0539 UT over a range of geomagnetic latitudes from $\lambda_m = 45^\circ\text{N}$ to $\lambda_m = 20^\circ\text{S}$ and L shells of $L = 4.3$ to $L = 5.3$. Electron density deduced from in situ and remote measurements indicates that during this time the DE 1 satellite was near the boundary of the plasmasphere. Observations can be summarized as follows: (1) The general character of the electric and magnetic field spectrum remained the same throughout the 3-hour-long period, exhibiting an intensity peak at 1550 Hz. (2) The intensities of both the electric and the magnetic field decreased during this interval by ~ 30 dB. (3) Well-defined fading patterns at half the spin period (3.04 s) were observed throughout this period. These patterns were stable over a time scale of ~ 1 min. (4) In addition, a slow fading pattern with a time scale of 30 s was observed approximately 30% of the time. (5) The hiss intensity also showed fading over a time scale of ~ 10 –15 min. The spin fading patterns led to the measurement of wave propagation direction(s). The results of our analysis can be summarized as follows: (1) Near the geomagnetic equator (within $\sim \pm 3^\circ$ latitude) we observe a wave normal angle of $60^\circ \pm 5^\circ$ with respect to the local geomagnetic field. (2) Away from the equator, wave normal directions range from 30° to 80° with respect to the local geomagnetic field. (3) All wave normal directions observed over the 3-hour-long period were within $\sim \pm 45^\circ$ of the plane normal to the local magnetic meridional plane. Results indicate that the hiss source radiates with initial wave normal angles in the range $30^\circ < \theta_0 < \theta_g$ (Gendrin angle) and $90^\circ < \phi_0 < 270^\circ$, contrary to the common assumption that the source emits with wave normal angles closely aligned with the geomagnetic field. The FDF formulation has also permitted elucidation of the statistical nature of hiss. The slow time fading (~ 30 s) is interpreted in terms of a coherence bandwidth $\Delta\omega$ of about 0.2 rad/s.

1. INTRODUCTION

ELF/VLF hiss is a common example of broadband electromagnetic noise observed in planetary magnetospheres [Barrington *et al.*, 1963; Helliwell, 1965; Duncel and Helliwell, 1969; Russell *et al.*, 1969; Gurnett *et al.*, 1969; Scarf *et al.*, 1981]. Of particular interest for this paper are whistler mode hiss emissions, which are observed at frequencies below the local electron gyrofrequency f_H and the local plasma frequency f_P . In the Earth's magnetosphere, whistler mode hiss is observed at low altitudes ($\leq 2R_E$) in the auroral regions, where it is called auroral hiss, and also throughout much of the closed-field-line regions of the magnetosphere. Commonly observed within the plasmasphere, hiss can potentially play an important role in the dynamics of the radiation belts. Precipitation of energetic particles as a result of resonant interactions with waves in general is believed to be the dominant loss process for the radiation belts [Kennel and Petschek, 1966]. Interactions involving whistler mode hiss, in particular, have been suggested as being a primary factor in determining the morphology of the belts and the slot region [Lyons *et al.*, 1972]. On the other hand, recent experimental observations of burst electron precipitation by

lightning-generated whistlers [Voss *et al.*, 1984; Inan *et al.*, 1985; Inan and Carpenter, 1987] and VLF transmitter signals [Imhof *et al.*, 1983] indicate that discrete whistler mode signals other than hiss may play significant roles in determining the loss rates for the radiation belts at mid-to-low latitudes within the plasmasphere. Thus a detailed understanding of the generation, propagation, and maintenance of hiss is an important problem of magnetospheric physics.

An adequate understanding of hiss must involve (1) the characterization of hiss, (2) the nature and location of the source region(s), and (3) generation mechanisms. At present our understanding of hiss is lacking with respect to each of these aspects. The past studies of hiss can be categorized in three ways: (1) characterization of hiss based on occurrence, intensity, and spectral information [Duncel and Helliwell, 1969; Russell *et al.*, 1969; Thorne *et al.*, 1973], (2) characterization based on direction of arrival information [Hayakawa *et al.*, 1986; Lefeuvre *et al.*, 1981], and (3) theoretical work to explain the generation, maintenance, and propagation of hiss [Thorne *et al.*, 1973, 1979; Church and Thorne, 1983; Huang *et al.*, 1983].

Ground-based observations of hiss have been well documented by Helliwell [1965]. The first in situ observations of hiss were made on lower-altitude polar-orbiting satellites [Barrington *et al.*, 1963; Gurnett and O'Brien, 1964; Scarf *et al.*, 1968; Taylor and Gurnett, 1968]. Like ground observations, these observations provide only partial information about the waves in the magnetosphere due to reflection and

Copyright 1988 by the American Geophysical Union.

Paper number 7A9177.
0148-0227/88/007A-9177\$05.00

absorption of down coming waves at higher altitudes. High-altitude satellite measurements are necessary for a complete understanding of the physics of hiss generation and propagation in subauroral regions. Detailed morphological studies using data from the high-altitude OGO 1 and OGO 3 satellites were reported by *Dunckel and Helliwell* [1969] and *Russell et al.* [1969]. Subsequently, *Muzzio and Angerami* [1972] and *Thorne et al.* [1973] provided observations from the OGO 4 and OGO 5 satellites, respectively. *Smith et al.* [1974], and *Parady et al.* [1975] based studies on observations of hiss on OGO 6 and Explorer 45, respectively. These studies involved the morphology and occurrence patterns of hiss in different subauroral regions of the magnetosphere at all local times. The general conclusions of these initial studies can be summarized as follows:

1. Hiss is found throughout the plasmasphere and is stronger in the daytime sector compared to the midnight-to-dawn sector. Its broadband intensity or spectrum shows little or no systematic variation with L value; however, it often peaks at high ($>40^\circ$) latitudes. It often shows a sharp cutoff at the plasmapause, though it is also observed outside the plasmasphere [*Dunckel and Helliwell*, 1969; *Russell et al.*, 1969; *Thorne et al.*, 1973].
2. Hiss is observed in a frequency band ~ 100 Hz to ~ 3 kHz. The spectrum generally shows peak intensity at frequencies below 1 kHz.
3. It appears that the upper cutoff of hiss is controlled equatorially [*Dunckel and Helliwell*, 1969; *Muzzio and Angerami*, 1972], while the lower cutoff is controlled locally [*Muzzio and Angerami*, 1972; *Thorne et al.*, 1973].
4. Hiss intensity is correlated with magnetic substorm activity. It decreases soon after a substorm and builds up during the recovery phase. The detectable waves persist even during quiet periods [*Smith et al.*, 1974; *Parady et al.*, 1975].

The strength of wave-particle interactions in the magnetosphere is dependent on the wave normal directions of the whistler mode waves interacting with the particles. Earlier studies [*Kennel and Petschek*, 1966; *Thorne et al.*, 1973] assumed propagation parallel to Earth's magnetic field. *Kennel and Petschek* [1966] were successful in explaining pitch angle diffusion of energetic particles; however, the observed properties, in particular the intensity of VLF hiss, could not be explained. *Storey* [1971] suggested that a better understanding of these interactions must take into account the distributions of waves in frequency and direction as well as the distribution functions of particles. The need for the estimation of wave distribution in frequency and direction was reemphasized by *Shawhan* [1983] in connection with the future instrumentation on satellites. *Storey and Lefeuvre* [1974] developed a formulation to measure wave properties based on the concept of the wave distribution function, WDF, which could be used to represent random electromagnetic noise such as hiss. The WDF model assumes hiss to be a superposition of a large number of plane waves each having an infinitesimal amplitude and a random phase such that any two plane waves differing in either frequency or direction are mutually uncorrelated. *Storey and Lefeuvre* also developed techniques to measure the wave distribution functions of hiss observed on satellites [*Storey*, 1971; *Storey and Lefeuvre*, 1979]. Several studies based on these techniques have been presented using data available from ISEE 1 and the GEOS satellites [*Lefeuvre et al.*, 1983; *Lefeuvre and*

Helliwell, 1985; *Hayakawa et al.*, 1986; *Parrot and Lefeuvre*, 1986]. The general results from these studies are listed below.

1. Most often waves propagate with oblique wave normal angles.
2. About 40% of the time, waves show a double-peaked distribution; at other times they exhibit a broadly peaked distribution.
3. Even close to the geomagnetic equator, which is a favored region for the generation of hiss, waves are found to propagate with all possible wave normal directions.

It may be noted here that the above results are in apparent contradiction with the common assumption (see below) that strongest wave-particle interactions occur when the waves are propagating parallel to the geomagnetic field.

On the theoretical side the most noted works are those of *Kennel and Petschek* [1965], *Lyons et al.* [1972], *Thorne et al.* [1973, 1979], *Church and Thorne* [1983], and *Huang et al.* [1983]. The earlier studies assumed hiss to be a plane wave propagating parallel to the Earth's magnetic field and the wave-particle interaction to take place near the equator. The main reason for this assumption was that the spatial growth rate is maximized under this condition [*Kennel and Petschek*, 1966]. It was found that the estimated gains are not sufficient to explain the observed intensities when hiss is assumed to be generated from ambient thermal noise. Later it was proposed [*Thorne et al.*, 1979; *Church and Thorne*, 1983] that the waves follow a cyclic path and that the noise is amplified each time it passes through the equatorial region with low wave normal angles. In general, 40–50 passes would be required for the waves to be amplified to the observed level. Based on path-integrated gain/loss calculations, *Huang et al.* [1983] showed that in general the waves would be damped out to thermal levels before being magnetospherically reflected. Therefore, the recycling model of *Thorne et al.* [1979] may not explain the amplification process. Another possibility suggested by *Church and Thorne* [1983] and by *Huang et al.* [1983], is that most of the waves are generated by a strong embryonic source, and that they subsequently propagate to the rest of the magnetosphere. The local gain/loss in this mechanism is used to explain either the maintenance or the eventual damping of hiss waves. Path-integrated gains needed for this purpose are naturally much smaller. In the context of the embryonic source model, the outstanding problems include the identification of source location(s) and the generation mechanism.

The present paper introduces a new and general formalism for analysis of whistler mode signals received on a spinning satellite. A specific method is developed and applied to the case of hiss signals observed on the DE 1 satellite. The major advantage of our data is that nearly simultaneous measurements of electric and magnetic fields are available for quantitative analysis over a relatively long satellite trajectory. For the case studied in this paper, on September 23, 1983, hiss was observed continuously over a ~ 3 -hour-long period over a wide range of geomagnetic latitudes. The spin of the satellite provides a natural way to measure the wave normal directions [*Sonwalkar*, 1986; *Sonwalkar and Inan*, 1986]. In situ measurements of cold plasma density and observations of Siple Station, Antarctica, transmitter signals are used to arrive at a reasonable model of the magnetospheric cold plasma density distribution at the time of measurements. Most past studies have been statistical in nature

and involved analysis of hiss received within relatively short periods (a few seconds) and/or at a limited number of points in space. In this paper, we present the first detailed study considering hiss as an enduring phenomenon and thus investigating relationships among the properties of hiss observed in different regions of the magnetosphere.

The organization of the paper is as follows. Section 2 describes the experimental setup and the data in terms of its spectral properties and the envelopes of the measured electric and magnetic field intensities along the nearly field-aligned satellite trajectory. Section 3 introduces a new formulation to analyze hiss data. Section 4 describes the measurement of wave normal direction. Section 5 discusses the results in the light of previous work on wave normal direction, source region, propagation, and the nature of hiss. Summary and conclusions are provided in section 6.

2. OBSERVATIONS

The data utilized in this paper were acquired in the course of VLF wave injection experiments carried out during August–December 1983 using the Stanford University VLF transmitter at Siple Station, Antarctica [Helliwell and Katsufakis, 1974], and the linear wideband receiver (LWR) on the Dynamics Explorer (DE 1) satellite. The LWR receiver is integrated into the Plasma Wave Instrument (PWI) on the DE 1 satellite [Shawhan *et al.*, 1981] and measures wave amplitude in the frequency range 1.5–16 kHz. The gain of the amplifier can be set at 10-dB steps over a 70-dB range and can be varied automatically or can be commanded to remain fixed at any level. In the automatic mode the gain is reset every 8 s. The response is linear over a 30-dB range in any gain position, thus facilitating accurate measurement of signal intensity and temporal growth rate. The LWR can be commanded to cycle between a 200-m-long electric dipole or a 0.8 m by 1.25 m single-turn loop magnetic antenna (threshold sensitivity $6 \times 10^{-10} \gamma/(\text{Hz})^{1/2}$ at 6 kHz). The input impedance of the LWR preamplifier is $\geq 10^9 \Omega$. The main purposes of the wave injection experiments were to study the propagation, amplification, and emission triggering of natural signals as well as signals from the transmitter.

In this paper, we present an analysis of broadband whistler mode hiss emissions observed during 0236–0545 UT September 23, 1983, when the DE 1 satellite followed the trajectory shown in Figure 1, moving from $\lambda_m=45^\circ\text{N}$ to $\lambda_m=20^\circ\text{S}$, and between $L=4.3$ and $L=5.3$. Geomagnetic longitude varied from $\sim 10^\circ\text{E}$ to $\sim 33^\circ\text{W}$.

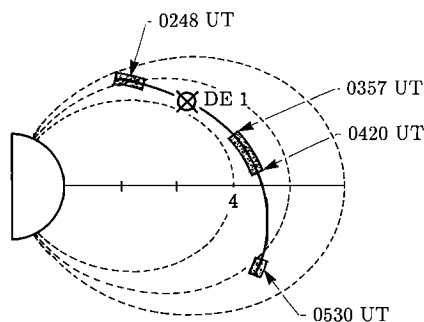


Fig. 1. Projection of the satellite trajectory onto the magnetic meridional plane on September 23, 1983, during 0242–0539 UT when a hiss band was observed continuously.

The choice of this particular data set for detailed study was somewhat arbitrary, except for the fact that the hiss signal was strong enough on both E_x and B antennas to permit a quantitative analysis over a 3-hour-long DE 1 trajectory (hiss showing similar features is commonly observed on satellites). On the other hand, the data acquired on this day are somewhat special, in that the satellite trajectory grazed the boundary of the plasmasphere.

In Plate 1 wave spectra from four regions along the satellite trajectory (shown in Figure 1a) illustrate typical signal characteristics, showing the hiss band, whistlers, and Siple transmitter signals. A hiss band between 1.0 kHz and 1.9 kHz was observed almost continuously during the 0236–0545 UT period. The lower cutoff is set by the LWR receiver which has a 3-dB lower cutoff at 1.5 kHz (in the rest of the analysis presented below, filter roll-off has been taken into account). Since, in general, hiss bands in the magnetosphere are regularly observed down to a few hundred hertz, it is possible that the hiss observed on September 23, 1983 was also present at frequencies much lower than the receiver cutoff.

2.1. Cold Plasma Density

In situ electron densities were deduced from the measurement of the upper hybrid resonance (UHR) on records of the University of Iowa sweep frequency receiver (SFR) (the electron density data were made available by courtesy of D. A. Gurnett and A. Persoon of the University of Iowa). The electron density varied along the satellite trajectory from ~ 60 to ~ 20 per cubic centimeter. Figure 2 shows the plot of the equatorial electron density deduced from UHR measurements. The equatorial electron density inferred from whistler measurements and time delay measurements of Siple transmitter signals are also shown in Figure 2. The reported cold plasma density values of 20–60 el/cm^3

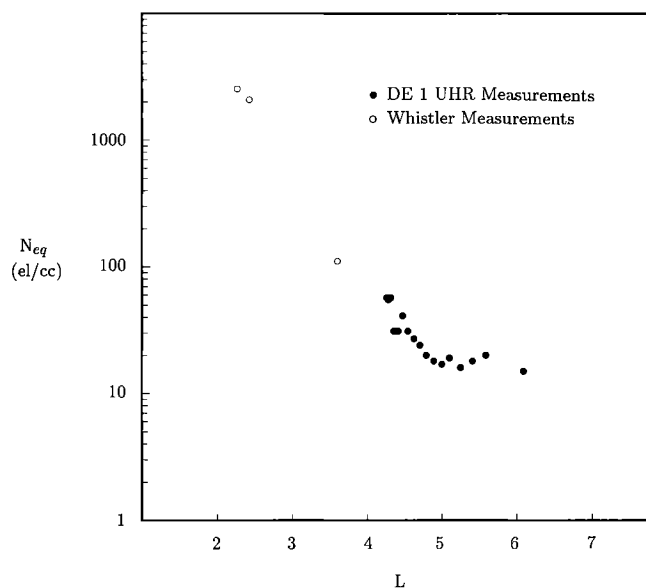


Fig. 2. Equatorial electron density deduced from the upper hybrid resonance noise measured with sweep frequency receiver on DE 1, time delay measurements of Siple signals on DE-1, and dispersion analysis on whistlers observed at Roberval, Quebec, and at Siple Station, Antarctica.

and the fact the observations were made during the multi-day recovery phase of a weak magnetic storm, suggest that the satellite was very close to the plasmapause boundary throughout this time.

2.2. Fading Patterns

Most of the quantitative analysis presented here is based on the measurement of the envelopes of hiss signal intensity. The signal is passed through a band-pass filter (Δf), centered on frequency f_c , followed by a square law envelope detector. The output amplitude of the resulting signal is then plotted on a strip chart recorder as a function of time. Usually, an integrator with integration time of 100–300 ms is used to smooth the data. Clearly, a large number of data sets can be collected by varying f_c and Δf . The rationale for processing data in this manner will be evident from the theory presented in the next section.

Figure 3 shows a few typical examples of hiss data processed as mentioned above, with $f_c = 1500$ Hz and $\Delta f = 300$ Hz. To make better measurements of both the maxima and the minima in fading patterns, the intensity is plotted in two panels: one giving accurate measurements of maxima (upper panel), and the other giving accurate measurements of minima (lower panel). Figure 3a shows hiss electric field intensity at 0242:32 UT; a well-defined and stable fading (13 dB) at twice the spin period (3.04 s) persisted throughout the minute covered. Figure 3b shows another example of hiss intensity observed at 0357:30 UT. The first ~ 30 s shows the magnetic field envelope, whereas the remaining part shows the electric field envelope. (We note that at any given time, depending on whether the E_x or the B antenna was connected to LWR, either electric or magnetic field (but not both) measurements were available. The position of the arrow in Figure 3 indicates when the E_x or the B antenna was connected to the LWR receiver.) These data, in addition to spin fading, show a slower fading over a time scale of 30 s. In Figure 3c, from 0436:50 UT, the electric field shows well-defined spin fading, while the magnetic field exhibits no significant fading. This type of fading was observed continuously in the September 23, 1983 data, during times when the satellite was within $\sim 3^\circ$ in latitude of the magnetic equator. Figure 3d shows the sudden reappearance of the spin fading in the magnetic field at 0439:38 UT ($\lambda_m \sim 3.5^\circ$). Finally Figure 3e, from 0537:11 UT at the southern end of the trajectory shown in Figure 1, again shows a stable and well-defined spin fading. Note that the absolute magnitude of electric field now is 30 dB below that at 0242 UT (Figure 3a); however, spin fading is still very clear. The sudden jumps in the amplitude at $\sim 0537:30$ and at $\sim 0537:45$ UT are due to the arrival of lightning-generated whistlers. In general, whistlers are easily identified in the amplitude data by examining the associated frequency-time spectrograms.

One of the most important features of these data is stable and well-defined fading patterns at $2\omega_s$ over a time scale of 1 min, with ω_s being the satellite spin frequency. The fading at twice the spin frequency was very pronounced in the electric field data throughout the ~ 3 -hour period of observation. It was also found in the magnetic field data, except for a region close to the equator. The other important feature is an additional slow time variation with a period of ~ 30 s. Substantial intensity variation over an ~ 30 -s time scale was observed about 30% of the time.

In the next section we present an interpretation of the spin fading in terms of the direction(s) of arrival of hiss signals at the satellite, including the case when no fading was seen on the magnetic field. The slower time variation is interpreted as a change in the source intensity, or alternatively, in terms of the statistical nature of hiss.

2.3. Signal Intensity

Figure 4 shows the measured hiss intensity along the satellite trajectory. Here we have plotted the electric and magnetic field intensity measured in a 300-Hz band centered around 1500 Hz. Note that the LWR was toggled between two antennae at irregular intervals so that at any given time either E_x or B data were available but not both. However, on average, the plotted points represent sample electric and magnetic field data at ~ 5 -min intervals. The fields plotted are the maximum intensities during each 5-min interval. From Figure 4, the following features are evident: (1) Both the electric and magnetic field intensities decreased by ~ 30 dB as the satellite moved from 45°N to 20°S geomagnetic latitude. (2) The electric and magnetic field intensities exhibited a fading pattern over a time scale of ~ 10 –15 min. We note here that such ~ 10 - to 15-min time scale fading patterns were also reported by Parady *et al.* [1975] from Explorer 45 data.

2.4. Frequency Range

Figure 5 shows (left) electric and (right) magnetic field amplitude spectra from three distinct regions along the trajectory. Region I is at ($L = 4.93$, $\lambda_m = 40^\circ\text{N}$), region II is near the equator at ($L = 4.47$, $\lambda_m = 2.3^\circ\text{N}$), and region III is on the other side of the equator at ($L = 5.23$, $\lambda_m = 20.2^\circ\text{S}$). These spectra were obtained from the signal envelope with $\Delta f = 100$ Hz, and f_c was varied from 1350 Hz to 1950 Hz in steps of 100 Hz. The data represent averages over a 2-min interval. For frequencies below the LWR cutoff, the known filter roll-off was compensated for. It is evident from this figure that the general nature of the spectrum remained similar throughout the 3-hour-long DE 1 trajectory. All the spectra exhibit a peak at 1550 Hz.

2.5. Summary of the Observations

The salient features of the hiss phenomena observed on September 23, 1983, are summarized below.

1. Hiss was continuously observed over at least a ~ 3 -hour period.
2. Hiss was mainly observed between 1.0 and 1.8 kHz. The lower cutoff is an artificial one, since the LWR filter has a 3-dB cutoff at 1.5 kHz. The measurements at 1.0 kHz along with the LWR filter roll-off suggest that the hiss band extended below 1.0 kHz. Thus it is possible that the observed emission was plasmaspheric hiss, which typically is observed to extend to frequencies as low as ~ 100 Hz [Thorne *et al.*, 1973].
3. Stable and well-defined fading patterns at $2\omega_s$ over a time scale of 1 min were observed throughout the measurement, where ω_s is the satellite spin frequency. The spin period of the DE 1 satellite is 6.08 s/revolution.
4. An additional slow time variation with a period of ~ 30 s was also observed about 30% of the time.
5. There was consistent fading in the observed electric and magnetic field data over a time scale of ~ 10 –15 min.

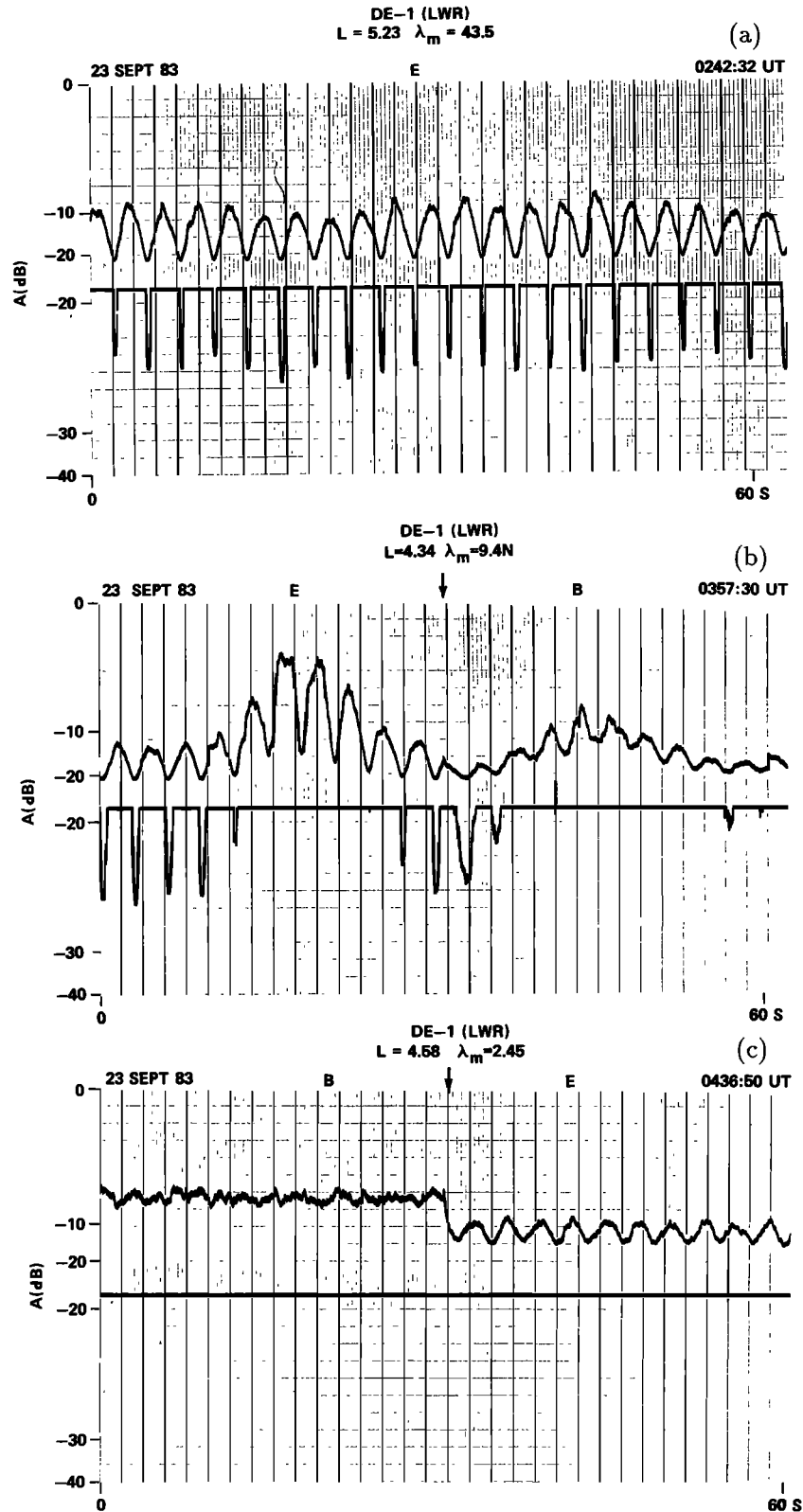


Fig. 3. Examples of fading patterns observed in the hiss data. (a) Well-defined and stable fading at $2\omega_s$ is seen in the electric field data at 0242:32 UT for 1 min. Spin fading is seen in electric field data for the entire 3-hour-long period. (b) Shows spin fading in the electric and magnetic field data at 0357:30 UT. The LWR was toggled from the electric to the magnetic antenna at the time indicated by an arrow. Observe a slow fading in both the electric and magnetic data of period ~ 30 s. This type of fading was seen $\sim 30\%$ of the time. (c) Fading seen at 0436:50 UT near equator. We see almost no fading in the magnetic field data and relatively little fading in the electric field data. This type of fading was seen continuously within a few degrees latitude from the geomagnetic equator. (d) Fading at 0439:02 UT. Note that a sudden spin fading appears in the magnetic field data at $\sim 0439:40$ UT. (e) Spin fading in the electric field data seen at 0537:11 UT. The absolute magnitude of electric field now is 30 dB below that at 0242 UT (Figure 3a); however, spin fading is still very clear. Sudden amplitude jumps at 0537:30 and 0537:40 are due to whistlers.

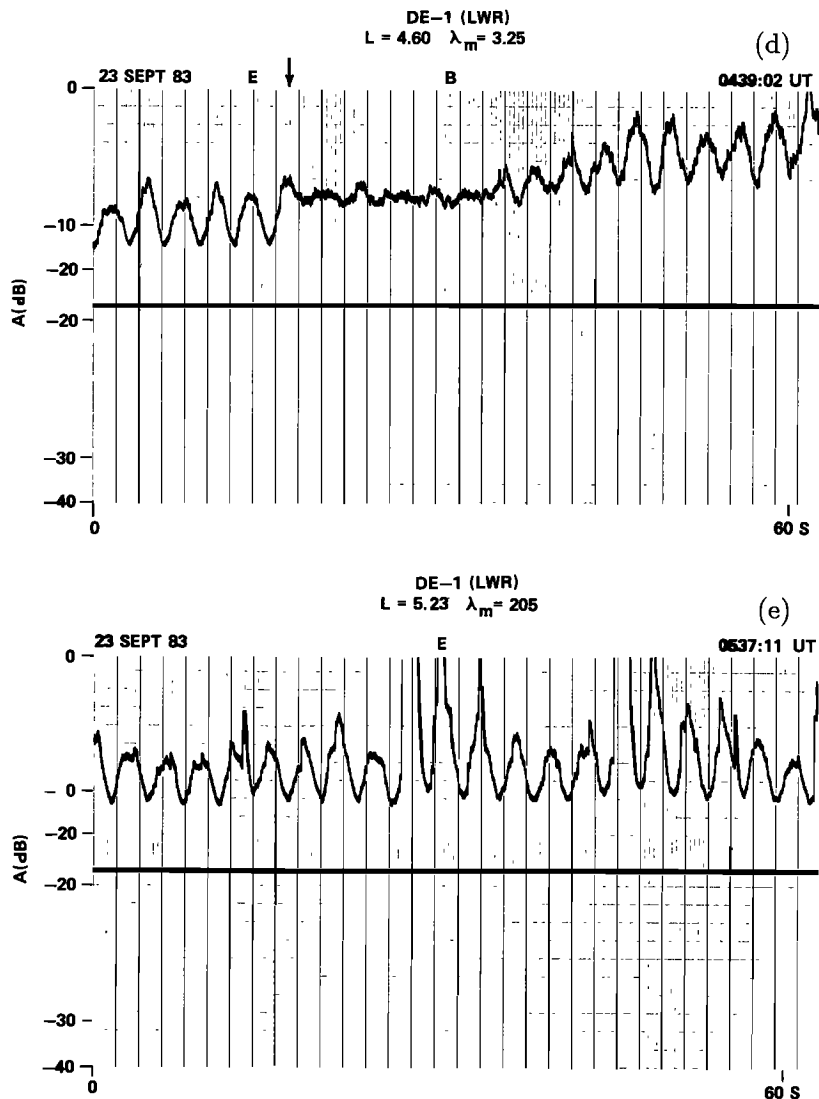


Fig. 3. (continued)

6. The general nature of the electric and magnetic field spectrum was unchanged throughout the 3-hour-long DE 1 trajectory.

The consistency of the fading patterns (all three time scales listed above) as well as the similarity of the spectra over the entire 3-hour-long trajectory suggests that the hiss can be considered as a spatially and temporally enduring phenomenon. This realization facilitates and helps to justify the new analysis technique presented below.

3. A MODEL FOR HISS AND A NEW METHOD TO MEASURE ITS WAVE NORMAL DIRECTION

In this section we present a new method to analyze wide-band hiss signals observed on a spinning satellite. The method is based on a formalism developed to analyze satellite wave data [Sonwalkar, 1986]. This formalism takes into account the kinematic constraints resulting from the spinning and linear motion of the satellite, and the kinetic constraints arising from the medium properties, to relate the

voltage received to the wave field structure to be determined. An application of this formalism to determine the wave normal directions of ground transmitter signals received on the DE 1 and ISEE 1 satellites has appeared in previous papers [Sonwalkar *et al.*, 1984; Sonwalkar and Inan, 1986]. It also led to the first in situ measurement of the effective length of a dipole antenna aboard the DE 1 satellite [Sonwalkar and Inan, 1986]. In this section we extend the formalism to the particular problem of analysis of hiss for the purpose of measuring its wave normal direction(s) and coherence properties.

3.1. Modeling the Hiss: Field Distribution Function (FDF)

An arbitrary electromagnetic field present in some region of space Δr centered around r_0 during an interval Δt can be decomposed into its Fourier transform:

$$E(r, t) = \int_{\omega} \int_{\mathbf{k}} E_0(\mathbf{k}, \omega) e^{i(\omega t - \mathbf{k} \cdot \mathbf{r})} d\mathbf{k} d\omega \quad (1)$$

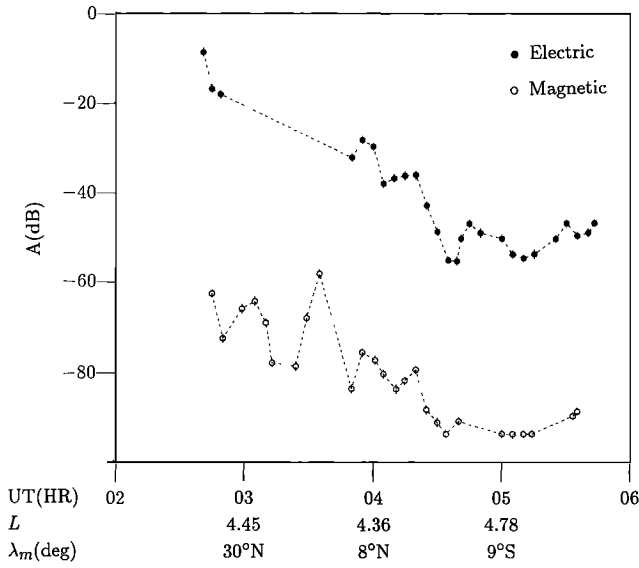


Fig. 4. Electric and magnetic field intensities during the entire 3-hour-long trajectory. Both electric and magnetic field decrease by ~ 30 dB during this interval. Note that a fading at the ~ 10 - to 15 -min time scale is observable in both the electric and magnetic field data; 0 dB in this figure corresponds to either $10 \mu\text{V/m}$ or $20 \text{ pT/Hz}^{1/2}$.

The resolution in k and ω is of the order of $1/\Delta r$ and $1/\Delta t$, respectively. The choice of $(\Delta r, \Delta t)$ is dependent on the specific phenomenon to be studied and the environment of the experiment. Our interest here is to model VLF/ELF hiss observed in the Earth's magnetosphere. It is well known that in the inner magnetosphere and at frequencies in the few kilohertz range the whistler mode is the only propagating cold plasma wave mode. This fact is recognized and is included quantitatively in our analysis. The easiest way to achieve this is to explicitly incorporate whistler mode plane wave polarization and dispersion relations in equation (1). To do this, however, we must have a uniform magnetoplasma, i.e., uniform B_0 and n_e over the interval $(\Delta r, \Delta t)$. Based on the past satellite measurements of B_0 and n_e and observations of fixed frequency ground transmitter signals [Sonwalkar et al., 1984; Sonwalkar and Inan,

1986] as well as hiss signals reported here, the medium can usually be considered uniform for propagation effects over a time scale of ~ 1 min and a length scale of a few hundred kilometers. It may be noted here that the above assumption is needed in order to represent the signal in the magnetosphere in a consistent manner. The considerations related to the measurement process will be treated in the next subsection. Signals with wave energy extending in space beyond Δr will be represented in blocks centered around $r_0 \pm \Delta r$, where r_0 is shifted appropriately such that the medium can be considered uniform during any one interval. Similarly a wave phenomenon persisting in time longer than Δt will be treated in blocks centered around $t_0 \pm \Delta t$, where t_0 is shifted in time. In each of these blocks the medium can be considered slowly varying. This method of representing the signal is reasonable, particularly in the case of whistler mode propagation, for which numerous earlier studies have demonstrated that a WKB-based ray propagation model provides a fairly accurate description of the wave propagation in the magnetosphere.

For a plane whistler mode wave, the polarization and wave normal vector are known functions of (θ, ϕ, ω) , provided the local B_0 and n_e are uniform in space and time. Thus, the electric field of an arbitrary whistler mode signal can be described as follows (see Appendix).

$$\mathbf{E}(\mathbf{r}, t) = \int_{\omega} \int_{\theta} \int_{\phi} E_0(\theta, \phi, \omega) \mathbf{R}^e(\theta, \phi, \omega) \cdot e^{[i(\omega t - \mathbf{k}(\theta, \phi, \omega) \cdot \mathbf{r})]} d(\cos \theta) d\phi d\omega \quad (2)$$

where $\mathbf{R}^e(\theta, \phi, \omega)$ and $\mathbf{k}(\theta, \phi, \omega)$ are the whistler mode polarization and wave normal vectors respectively [Stix, 1962]. Now $|d\sigma| = |d(\cos \theta) d\phi| = |\sin \theta d\theta d\phi|$ is the element of solid angle corresponding to the intervals from θ to $\theta + d\theta$ and from ϕ to $\phi + d\phi$. For brevity we represent the direction (θ, ϕ) by a unit vector \mathbf{u} in that direction. Then the equivalent expression to equation (1) is

$$\mathbf{E}(\mathbf{r}, t) = \int_{\omega} \oint_{\sigma} E_0(\mathbf{u}, \omega) \mathbf{R}^e(\mathbf{u}, \omega) \cdot e^{[i(\omega t - \mathbf{k}(\mathbf{u}, \omega) \cdot \mathbf{r})]} d\sigma d\omega \quad (3)$$

For consistency, it is required that the measurements be performed over time scales and length scales which are much larger than $(2\pi/\omega)$ and $(2\pi/k)$ respectively, and over which the medium parameters are uniform. For the choice of Δt made above, these conditions are easily satisfied. The main advantage of (2) or (3) over (1) is that for a given mode, $\mathbf{R}^e(\theta, \phi, \omega)$ and $\mathbf{k}(\theta, \phi, \omega)$ are known functions of (θ, ϕ, ω) . In other words, (2) and (3) allow us to explicitly include the prior information in our formulation. This advantage is, of course, gained at the expense of limiting the range of analysis to $(\Delta r, \Delta t)$, or equivalently, limiting the resolution in k and ω .

The wave magnetic field is deducible directly from (3) by using the Maxwell's equation and whistler mode relations:

$$\mathbf{B}(\mathbf{r}, t) = \int_{\omega} \oint_{\sigma} E_0(\mathbf{u}, \omega) \left[\frac{\mathbf{k} \times \mathbf{R}^e(\mathbf{u}, \omega)}{\omega} \right] \cdot e^{[i(\omega t - \mathbf{k}(\mathbf{u}, \omega) \cdot \mathbf{r})]} d\sigma d\omega \quad (4)$$

We call $E_0(\theta, \phi, \omega)$, or equivalently $E_0(\mathbf{u}, \omega)$, the field distribution function (FDF), by analogy to the previously

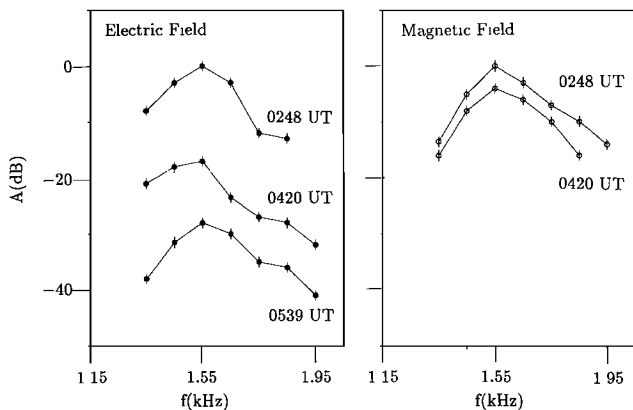


Fig. 5. Electric and magnetic field spectrum at three different times. The general nature of the spectrum remains similar throughout the 3-hour-long trajectory showing a peak at 1550 Hz.

introduced wave distribution function (WDF) [Storey and Lefeuvre, 1974]. It can be seen from equations (2)–(4) that the FDF completely represents an arbitrary whistler mode wave propagating in a uniform magnetoplasma. There are two possible ways to assign further meaning and restriction to the FDF. In some cases it is better to think of the FDF as a deterministic representation of a signal under consideration. As an example, the FDF for a plane wave of frequency ω_0 and propagating in the direction (θ_0, ϕ_0) is given by

$$E_0(\theta, \phi, \omega) = E_0(\theta, \phi, \omega) \cdot \delta(\cos \theta - \cos \theta_0) \delta(\phi - \phi_0) \delta(\omega - \omega_0) \quad (5)$$

A ground transmitter signal at constant frequency can also be deterministically represented with a FDF (appendix, equation (A7)).

Some signals such as whistler mode hiss have a rather structureless spectrum, which suggests a statistical model for the corresponding FDF. In this case both the amplitude and the phase of the FDF are thought of as random variables, and the various ensemble averages are used to represent the signal. Additional restrictions on the FDF can be placed if more information is available. Thus for band-limited whistler mode hiss we have

$$E_0(\theta, \phi, \omega) = 0 \quad \theta > \theta_r, \quad \omega < \omega_l, \quad \omega > \omega_u \quad (6)$$

where θ_r is the resonance cone angle and the ω_l and ω_u are the lower and upper frequency cutoffs. Here, the direction cutoff comes from the whistler mode theory, whereas the frequency cutoffs can be taken to be the observed lower and upper cutoffs of hiss. $E_0(\theta, \phi, \omega)$ in equation (6) is a random variable and can be further specified by providing models for ensemble averages $\langle E_0(\theta, \phi, \omega) \rangle$ and $\langle E_0(\theta, \phi, \omega) E_0^*(\theta', \phi', \omega') \rangle$.

FDF representation is different than the local Fourier representation as well as the WDF representation. The appendix gives the formal relation between these three representations and elucidates the differences. Here, we note that the FDF and WDF represent fundamentally different quantities. The following differences deserve special attention. (1) The WDF is a point function and represents the ensemble average energy per unit volume in the element $d\sigma d\omega$ with frequency ω and direction (θ, ϕ) at a given point \mathbf{r} in space; thus the WDF varies from point to point in space. In particular, when the WDF is extracted from satellite wave data, the satellite motion cannot be accounted for. The FDF represents the wave structure present over a region $(\Delta \mathbf{r}, \Delta t)$ around some nominal point (\mathbf{r}_0, t_0) . In particular, the FDF represents the amplitude parameter of a plane wave with frequency ω and direction (θ, ϕ) . The overall structure is given by equation (2) or (3). In our formulation the satellite motion (spin and linear) is explicitly taken into account. (2) Unlike the WDF which is always ≥ 0 , the FDF is a complex function and has an amplitude as well as phase. Later, we show that the phase of the FDF plays a crucial part in the development of the concept of the coherence bandwidth of hiss. In the Storey and Lefeuvre formulation, using the WDF, the hiss is represented as a superposition of plane waves of infinitesimal amplitude propagating with different frequencies and wave normal directions and lacking mutual coherence; in other words, the statistical nature of hiss is assumed a priori. In our formulation, both the amplitude and phase of the FDF can be treated as random variables, and

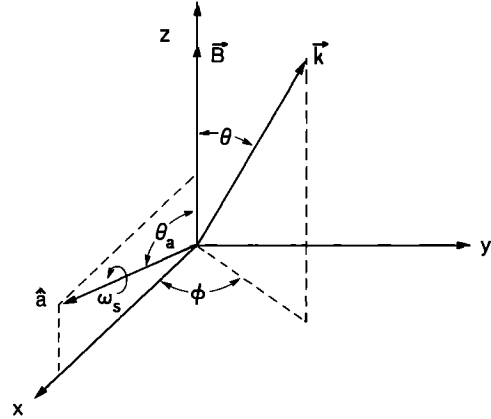


Fig. 6. Local coordinate system in space. \mathbf{B}_0 and \mathbf{k} are the local geomagnetic field and the wave vector, respectively, and \mathbf{a} is the spin axis of the spacecraft.

the statistical nature of hiss can be consistently determined from the data, as discussed in a later subsection. The appendix presents a detailed treatment of the relation between the FDF, Fourier, and WDF representations.

3.2. Voltages Measured on the Satellite

In this section we relate the FDF to the voltages measured at the terminals of the E_x or B antennae on a satellite by taking into account both the linear and the spin motion of the satellite. For the sake of brevity we consider the particular case of the DE 1 satellite, which is equipped with single electric and magnetic antennae. The general case of measurements with three electric and three magnetic antennae is treated elsewhere [Sonwalkar, 1986].

Consider a wideband signal received by single electric and magnetic dipole antennae on a spinning satellite (DE 1) at high altitudes in the magnetosphere (Figure 1). The coordinate system is described in Figure 6, where the z axis is taken to be along the Earth's magnetic field \mathbf{B}_0 , the spin axis \mathbf{a} is contained in the xz plane, and the y axis is given by the right-hand rule. For the case considered in this paper the yz plane is also the magnetic meridional plane, i.e., the spin axis is almost normal to the local meridional plane. Figure 7 shows the position of the antennae in a coordinate system (p, q, a) . The unit vectors along three axes are given by

$$\begin{aligned} \mathbf{p} &= \cos \theta_a \mathbf{x} - \sin \theta_a \mathbf{z} \\ \mathbf{q} &= \mathbf{y} \\ \mathbf{a} &= \sin \theta_a \mathbf{x} + \cos \theta_a \mathbf{z} \end{aligned} \quad (7)$$

Both antennae spin about the spin axis at an angular velocity ω_s . Also note that at any given time both antennae measure the field components along the same direction. The reference time t_r is taken to be the time when the electric dipole and the axis of the magnetic loop are aligned along the p axis. The phase α_{sp} of the antenna in the spin plane is the angle between \mathbf{l} and \mathbf{p} , where \mathbf{l} is a unit vector parallel to the length of the dipole antenna (or axis of the magnetic loop).

The instantaneous voltage induced at the terminals of a small linear electric dipole in the presence of an electric field \mathbf{E} is

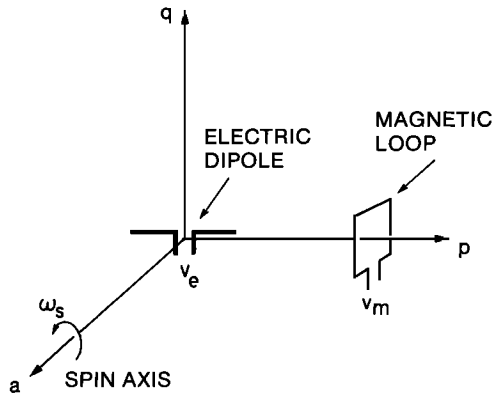


Fig. 7. Schematic of the antenna orientation in the spin plane. The spacecraft coordinate system is defined by equation (7). Electric and magnetic antennae spin at the frequency ω_s rad/s in the spin plane measuring the components of electric and magnetic fields. The length of the electric dipole and the axis of the magnetic loop are pointing in the same directions as they spin.

$$V^e = L_{\text{eff}} \mathbf{E} \cdot \mathbf{l} \quad (8)$$

where L_{eff} is the effective length of the dipole and \mathbf{l} is a unit vector parallel to the length of the antenna. For the DE 1 satellite electric field antenna $L_{\text{eff}} \sim 200$ m [Sonwalkar and Inan, 1986]. In equation (8) it is assumed that $L \ll \lambda$, where L is the physical length of the antenna and λ is the wavelength (in the magnetosphere). Therefore the phase and the magnitude of the signal along the length of the antenna are constant. When $L \sim \lambda$ we need to include the antenna interference pattern [Sonwalkar, 1986].

Similarly, the voltage induced across a small magnetic loop in the presence of a magnetic field \mathbf{B} is given by

$$V^m = S_{\text{eff}} \mathbf{B} \cdot \mathbf{n} \quad (9)$$

where S_{eff} is the effective length (aperture) of the magnetic loop and \mathbf{n} is normal to the loop. For the DE 1 satellite magnetic loop, \mathbf{n} is parallel to \mathbf{l} , i.e., both the electric and magnetic antennae measure E and B field components in the same direction at any given time. For the magnetic loop on the DE 1 satellite, $S_{\text{eff}} = (10^6 f / 1.081)$, where f is the frequency in hertz. Voltage V^m and magnetic field \mathbf{B} in equation (9) are in volts and teslas respectively.

The voltage received on a satellite moving with velocity \mathbf{v} and spinning with an angular velocity ω_s is given by

$$V^e(t) = \int_{\omega} \oint_{\sigma} d\sigma d\omega \left[\frac{E_0(\mathbf{u}, \omega) L_{\text{eff}}}{2} \right] \cdot \left[a_+(\mathbf{u}, \omega) e^{[i(\omega_d(\mathbf{u}, \omega) + \omega_s)t]} + a_-(\mathbf{u}, \omega) e^{[i(\omega_d(\mathbf{u}, \omega) - \omega_s)t]} \right] \quad (10)$$

where

$$a_{\pm} = (\mathbf{p} \mp i\mathbf{q}) \cdot \mathbf{R}^e \quad (11a)$$

and

$$\omega_d = (\omega - \mathbf{k} \cdot \mathbf{v}) \quad (11b)$$

where \mathbf{v} , ω_s , and ω_d are the satellite velocity, the spin

frequency, and the Doppler-shifted wave frequency, respectively.

The expressions for voltages across the magnetic field antenna are obtained by replacing L_{eff} by S_{eff} and a_{\pm} by b_{\pm} :

$$V^m(t) = \int_{\omega} \oint_{\sigma} d\sigma d\omega \left[\frac{E_0(\mathbf{u}, \omega) S_{\text{eff}}}{2} \right] \cdot \left[b_+(\mathbf{u}, \omega) e^{[i(\omega_d(\mathbf{u}, \omega) + \omega_s)t]} + b_-(\mathbf{u}, \omega) e^{[i(\omega_d(\mathbf{u}, \omega) - \omega_s)t]} \right] \quad (12)$$

$$b_{\pm} = (\mathbf{p} \mp i\mathbf{q}) \cdot \left(\frac{\mathbf{k} \times \mathbf{R}^e}{\omega} \right) \quad (13)$$

3.3 Connection Between Signal Spectrum and FDF

For a better understanding of the observation process it is useful to find the relation between the Fourier transform of the signal and the FDF. The Fourier transform, $V(\omega_r)$, of the received voltage is related to $V^e(t)$ as

$$V^e(t) = \int_{-\infty}^{\infty} V(\omega_r) e^{[i\omega_r t]} d\omega_r \quad (14)$$

The subscript r in ω_r is introduced to differentiate between the signal frequency and the frequency in the FDF. Thus

$$V^e(\omega_r) = \int_{\omega} \oint_{\sigma} d\sigma d\omega (E_0(\mathbf{u}, \omega) L_{\text{eff}}) \cdot [a_+(\mathbf{u}, \omega) \delta(\omega_r - \omega_d(\mathbf{u}, \omega) - \omega_s) + a_-(\mathbf{u}, \omega) \delta(\omega_r - \omega_d(\mathbf{u}, \omega) + \omega_s)] \quad (15)$$

From equation (15) we see that the contribution to the signal at frequency ω_r comes from all those plane wave components which satisfy the following relation:

$$\omega_d(\mathbf{u}, \omega) \pm \omega_s = \omega_r \quad (16)$$

Equation (16) describes two surfaces in the (θ, ϕ, ω) space. It is useful to introduce the concept of surfaces of constant Doppler frequency as they play a central role in the analysis of the data received on a spacecraft [Sonwalkar, 1986]. These are defined as

$$\omega_d(\mathbf{u}, \omega) = \omega_d(\theta, \phi, \omega) = \text{const} \quad (17)$$

The important point to note is that for a given wave mode and spacecraft velocity \mathbf{v} , the surfaces of constant Doppler shift are known functions of (θ, ϕ, ω) . Since they are not dependent on antenna orientation or the response functions, the same Doppler surfaces will appear in the expressions for voltages across each of the antenna terminals.

3.4 Direct and Inverse Problems

The direct problem can be stated as follows: given the FDF $E_0(\mathbf{u}, \omega)$, find the voltages introduced across the electric and magnetic antennae, assuming whistler mode propagation. In equations (10) and (12), for a given mode, the coefficients a_{\pm} , b_{\pm} and the Doppler-shifted frequency ω_d are known functions of (θ, ϕ, ω) . Thus the expressions within the square brackets are known functions of (\mathbf{u}, ω) . Hence, equations (10) and (12) are the solutions of the direct problem.

The inverse problem is stated as follows: given the measured voltages, $V^e(t)$ and $V^m(t)$ over a time interval Δt , find the actual FDF $E_0(\mathbf{u}, \omega)$ that represents the distribution of whistler mode plane waves in $(\Delta \mathbf{r}, \Delta t)$. The inverse problem is ill-posed in the sense that it does not have a unique answer. The easiest way to see this is to look at equation (15), which states that FDF cannot be resolved on a constant Doppler surface. Statistical estimation methods, such as maximum entropy estimation or maximum likelihood estimation, are often used to find a unique answer to an ill-posed problem [Lefeuve *et al.*, 1981]. We shall in the next subsection provide a new method to find the average wave normal direction and to estimate the spread of the FDF in the (θ, ϕ) plane from the measured spin fading of received voltages $V^e(t)$ and $V^m(t)$.

3.5. A method to measure the wave normal direction of hiss

A general method to deduce wave normal directions from the measurement of six voltages, namely, three across electric antennae terminals and three across magnetic loops, is given by Sonwalkar [1986]. For technical reasons, the method developed here deals with the envelopes of the received voltages instead of the voltages directly. The main reason for this is that the wideband wave data acquired in the case of the DE 1 satellite (and also the ISEE 1 satellite) are in analog form and are stored on magnetic tapes. In the playback mode, it is generally found that the data have been distorted by tape flutter (of a few hertz) of random nature. Since the effect of tape flutter on signal frequency is directly proportional to frequency, it has little effect on the signal envelope [Sonwalkar, 1986]. Another reason why it is preferable to work with the signal envelopes is that any rapid fluctuations arising from local noise generation tend to cancel out. From equation (10), it can be seen that the envelope of the received voltage across a spinning electric field antenna aboard the satellite is given by

$$\begin{aligned} \overline{V^e(t)V^{e*}(t)} = & \int_{\omega} \int_{\omega'} \oint_{\sigma} \oint_{\sigma'} \left[\frac{E_0(\mathbf{u}, \omega) E_0^*(\mathbf{u}', \omega') L_{\text{eff}}^2}{4} \right] \\ & \cdot \left[(a_+(\mathbf{u}, \omega) a_+^*(\mathbf{u}', \omega') \right. \\ & + a_-(\mathbf{u}, \omega) a_-^*(\mathbf{u}', \omega') \\ & + a_+(\mathbf{u}, \omega) a_-^*(\mathbf{u}', \omega') e^{i2\omega_s t} \\ & \left. + a_-(\mathbf{u}, \omega) a_+^*(\mathbf{u}', \omega') e^{-i2\omega_s t} \right] \\ & \cdot e^{[i(\omega_d(\mathbf{u}, \omega) - \omega_d(\mathbf{u}', \omega'))t]} \\ & \cdot d\sigma d\sigma' d\omega d\omega' \end{aligned} \quad (18)$$

where the coefficients a_{\pm} are functions of spin axis orientation and whistler mode polarization relations. The overbar on the left-hand side indicates time averaging over fast variations. Note also that a_{\pm} and ω_d are known functions of the wave normal direction (θ, ϕ) and frequency ω . Equation (18) is the basis of wave normal analysis of hiss presented in this paper. The inverse problem of deducing FDF from equation (18) is ill-posed. However, with certain reasonable physical assumptions it becomes possible to estimate the "average" wave normal direction(s). As mentioned before,

we can treat the FDF as a random variable, and thus it is possible to deduce the statistical (ensemble) averages that can be related to measured quantities. The first assumption we make about FDF statistics is that the individual plane waves lack mutual coherence. Mathematically this can be expressed as

$$\langle E_0(\mathbf{u}, \omega) E_0^*(\mathbf{u}', \omega') \rangle = \langle E_0(\mathbf{u}, \omega) E_0^*(\mathbf{u}, \omega) \rangle \cdot \delta(\mathbf{u} - \mathbf{u}') \delta(\omega - \omega') \quad (19)$$

With this assumption we get

$$\begin{aligned} \langle \overline{V^e(t)V^{e*}(t)} \rangle = & \int_{\omega} \oint_{\sigma} \left[\frac{\langle E_0(\mathbf{u}, \omega) E_0^*(\mathbf{u}, \omega) \rangle L_{\text{eff}}^2}{4} \right] \\ & \cdot \left[(a_+(\mathbf{u}, \omega) a_+^*(\mathbf{u}, \omega) \right. \\ & + a_-(\mathbf{u}, \omega) a_-^*(\mathbf{u}, \omega) \\ & + a_+(\mathbf{u}, \omega) a_-^*(\mathbf{u}, \omega) e^{i2\omega_s t} \\ & \left. + a_-(\mathbf{u}, \omega) a_+^*(\mathbf{u}, \omega) e^{-i2\omega_s t} \right] d\sigma d\omega \end{aligned} \quad (20)$$

The quantities within angle brackets in equations (19) and (20) represent ensemble averages. Equation (20) states that subject to the assumption given by (19) the ensemble average of the voltage envelope has a precise sinusoidal variation at twice the spin frequency, i.e., at $2\omega_s$. Most experiments in space do not permit repetition, and thus we have to deal with one sample of data at any given time. The connection between the ensemble-averaged envelope and the actual envelope obtained from experiment is made with the help of an additional assumption: The actual measured voltage envelope is very close to that given by (20). In statistical mechanics this is called the "ergodic assumption." The validity of this assumption can be tested only experimentally. The necessary condition in our case is that the observed voltage show predominant fading at twice the spin frequency only. The data presented in this paper show that this is indeed the case. The reasons for this situation may be that (1) in some bandwidth $\Delta\omega$ and $(\Delta\theta, \Delta\phi)$, the magnitude of FDF, $E_0(\theta, \phi, \omega)$, is constant, and different plane waves arrive at the observation point in random phase, and (2) a_{\pm} are slowly varying functions of (θ, ϕ, ω) . From here onward we consider equation (20) to also represent the relation between the observed voltage envelope and the FDF.

This equation can be rewritten as follows:

$$\langle \overline{V^e(t)V^{e*}(t)} \rangle = \text{Re}[S_0^e + S_{2\omega_s}^e e^{i2\omega_s t}] \quad (21)$$

where

$$\begin{aligned} S_0^e = & \int_{\omega} \oint_{\sigma} \left[\frac{\langle E_0(\mathbf{u}, \omega) E_0^*(\mathbf{u}, \omega) \rangle L_{\text{eff}}^2}{4} \right] \\ & \cdot \left[a_+(\mathbf{u}, \omega) a_+^*(\mathbf{u}, \omega) \right. \\ & \left. + a_-(\mathbf{u}, \omega) a_-^*(\mathbf{u}, \omega) \right] d\sigma d\omega \end{aligned} \quad (22a)$$

$$S_{2\omega_s}^e = 2 \int \int_{\sigma} \left[\frac{\langle E_0(\mathbf{u}, \omega) E_0^*(\mathbf{u}, \omega) \rangle L_{\text{eff}}^2}{4} \right] \cdot [a_+(\mathbf{u}, \omega) a_-^*(\mathbf{u}, \omega)] d\sigma d\omega \quad (22b)$$

Equation (21) can be rewritten as follows:

$$\langle \overline{V^e(t) V^{e*}(t)} \rangle = A^e [1 + M^e \cos(2\omega_s t - \alpha^e)] \quad (23)$$

where $A^e = S_0^e$, $M^e = |(S_{2\omega_s}^e / S_0^e)|$, and $\alpha^e = \arg(S_{2\omega_s}^e)$. The experimentally measured parameters are S_0^e and $S_{2\omega_s}^e$, or alternatively A^e , M^e , and α^e . For a single-frequency wave arriving from one direction, these quantities are functions of (θ, ϕ) , antenna orientation, θ_a , α_s , and medium parameters. For a wide-band signal arriving from several directions they are a measure of the weighted "average" wave normal direction. Similar equations can also be written for the wave magnetic field. Thus, from one electric and one magnetic spinning antenna we get six measured parameters, namely, A^e , M^e , α^e , and A^m , M^m , and α^m which are weighted functions of parameters a_{\pm}^e and a_{\pm}^m . From equation (22) it may be noted that the fading parameters M^e , α^e , M^m , and α^m are insensitive to L_{eff} and S_{eff} , provided the latter are constant over the bandwidth $\Delta\omega$ under consideration. For this reason we shall use only these four parameters to define average wave normal direction.

One-region model: "Average" wave normal directions. Let us first consider what we mean by "average" wave normal direction. Consider hiss arriving from the directions which can be specified by a region $(\Delta\theta, \Delta\phi)$ in (θ, ϕ) space. With each (θ, ϕ, ω) we can assign $a_{\pm}^e(\theta, \phi, \omega)$, $b_{\pm}^e(\theta, \phi, \omega)$ and an amplitude parameter $E_0(\theta, \phi, \omega)$. The measured fading parameter gives the average of this distribution which in turn gives us an average wave normal (θ_0, ϕ_0) which lies in the $(\Delta\theta, \Delta\phi)$ region. The latter is easy to prove since all the weighting functions are positive.

Thus, the average wave normal direction is the solution of the following equations:

$$\begin{aligned} M^e(\theta, \phi) &= \overline{M^e} \\ \alpha^e(\theta, \phi) &= \overline{\alpha^e} \end{aligned} \quad (24a)$$

$$\begin{aligned} M^m(\theta, \phi) &= \overline{M^m} \\ \alpha^m(\theta, \phi) &= \overline{\alpha^m} \end{aligned} \quad (24b)$$

where $\overline{M^e}$, $\overline{\alpha^e}$, $\overline{M^m}$, and $\overline{\alpha^m}$ are the measured fading parameters. In equation (24) we assume $\omega = \omega_c$, where ω_c is the center frequency of the hiss band under consideration. For $\Delta\omega \sim 100$ Hz, fading parameters are slowly varying functions of frequency, therefore this assumption is easily justified. The solutions to these equations can be obtained graphically. Note that each of these equations represents a contour in the (θ, ϕ) plane; on each contour one of the fading parameters assumes a constant value equal to a measured parameter. The point(s) of intersection represent(s) the average wave normal angle. The quantities on the left are supposed to have been averaged over the frequency range of the band. If both electric field and magnetic field, i.e., equations (24a) and (24b), give the same solution, then hiss can be considered to be arriving from one direction. In fact, the necessary condition for one average direction is that one or more simultaneous solutions exist to equations (24a) and (24b). At this point it may be noted that due to the symmetries in the whistler mode relations and the fact that the

spin axis is nearly perpendicular to the geomagnetic field, we get multiple solutions to the set of equations (24). Thus if (θ, ϕ) is a solution, then $(\theta, \pi - \phi)$ and $(\pi - \theta, \pi + \phi)$ are also solutions. The wave normal on the DE 1 satellite with two antennae and only envelope information available can be determined subject to this uncertainty. In general, if $(\Delta\theta, \Delta\phi)$ is large, i.e., if the waves are spread out in direction of arrival, the solutions obtained from electric and magnetic measurements will differ. This can be noted from the fact that the kernels for electric field in equation (20) are functions of a_{\pm} , whereas those for magnetic field would be functions of b_{\pm} (see equations (11a) and (13)). Thus, when we do not have a simultaneous solution to equations (24), the individual solutions given by electric and magnetic field fading measurements represent a spread in the direction of arrival of the hiss signal. It is possible for hiss to arrive predominantly from two distinct regions in the (θ, ϕ) plane; this case is dealt with below.

Two-region model. When the one-region model discussed above does not yield a solution, we can consider the case of hiss arriving from two distinct regions in the (θ, ϕ) plane. In such a case the electric and magnetic fading contours lead to regions of intersections in the (θ, ϕ) plane which do not overlap. As mentioned above, this can be interpreted as a spread in the wave normal directions. With measurements on two antennae it is possible to determine if we have a continuous spread of wave normals or alternately a double-peaked distribution of wave normals. The necessary condition for a double-peaked distribution is that the following equations be satisfied simultaneously for some $(\theta_1, \phi_1, \theta_2, \phi_2)$, where (θ_1, ϕ_1) and (θ_2, ϕ_2) represent two distinct regions where the FDF peaks:

$$\begin{aligned} M^e(\theta_1, \phi_1, \theta_2, \phi_2, r^e) &= \overline{M^e} \\ \alpha^e(\theta_1, \phi_1, \theta_2, \phi_2, r^e) &= \overline{\alpha^e} \\ M^m(\theta_1, \phi_1, \theta_2, \phi_2, r^m) &= \overline{M^m} \\ \alpha^m(\theta_1, \phi_1, \theta_2, \phi_2, r^m) &= \overline{\alpha^m} \end{aligned} \quad (25)$$

where (θ_1, ϕ_1) and (θ_2, ϕ_2) are the two average wave normal directions for the two regions and r^e and r^m represent the relative strength of the two waves. The fading quantities are defined as follows:

$$\begin{aligned} S_0^e &= S_{0,1}^e + r^e S_{0,2}^e \\ S_{2\omega_s}^e &= S_{2\omega_s,1}^e + r^e S_{2\omega_s,2}^e \\ S_0^m &= S_{0,1}^m + r^m S_{0,2}^m \\ S_{2\omega_s}^m &= S_{2\omega_s,1}^m + r^m S_{2\omega_s,2}^m \\ r^e &= \left(\frac{E_2}{E_1} \right)^2 \\ r^m &= \left(\frac{k_2}{k_1} \right)^2 r^e \end{aligned} \quad (26)$$

A practical procedure to solve (25) would be to start with the two average wave normal directions obtained from the one-wave model. The parameters r^e and r^m , which represent the relative strength of two waves, can be varied between 0.1 and 10. (If r^e and/or r^m are too small or too large, we have essentially the one wave-model.)

When measurements from more than two antennae are available, one can consider a FDF with a larger (>2) number of peaks.

TABLE 1. Satellite Trajectory Parameters

Time, UT	Altitude, km	L Shell	λ_m , deg	ϕ_m , deg
0243	11,192	5.23	43.5	9.7
0248	12,081	4.93	40.0	8.1
0253	12,929	4.72	36.8	6.7
0304	14,652	4.45	30.6	3.4
0324	17,321	4.30	21.4	358.0
0334	18,448	4.28	17.6	355.6
0348	19,812	4.31	12.4	351.9
0357	20,564	4.34	9.4	349.7
0409	21,420	4.40	5.6	346.9
0420	22,064	4.47	2.3	344.3
0424	22,265	4.50	1.1	343.4
0428	22,450	4.52	-0.1	342.5
0432	22,617	4.55	-1.2	341.5
0436	22,768	4.58	-2.4	340.6
0438	22,837	4.60	-3.0	340.2
0440	22,902	4.61	-3.5	339.7
0442	22,963	4.63	-4.1	339.3
0450	23,164	4.69	-6.4	337.5
0500	23,324	4.78	-9.2	335.4
0510	23,383	4.88	-12.0	333.2
0528	23,232	5.09	-17.1	329.5
0539	22,977	5.23	-20.2	327.4

3.6. Interpretation of Slow Time Variations: Statistical Characterization of Hiss

In the last section, hiss was assumed to be a superposition of plane waves of infinitesimal amplitude, and the phases of these wavelets were assumed to be independent and uniformly distributed in the range $(0, 2\pi)$. It was shown that with this and the ergodic assumption the envelope of the voltage received on a spinning satellite contains only a variation at $2\omega_s$. As shown in Figure 3b, we find that additional frequencies (~ 30 -s time scale variation) are observed. There are two alternate ways to account for these additional time variations in the signal envelope.

1. These variations may be due to a slowly varying source intensity. In that case our choice of Δt is too large, i.e., the fields are not describable over this time scale and the corresponding length scale $v\Delta t$. This choice of interpreting the slow variations requires that we choose Δt less than our initial time scale of ~ 1 min, but larger than half the spin period (~ 3 s). Thus a choice of ~ 10 – 20 s would seem appropriate. Since the fading properties at $2\omega_s$ do not change appreciably over the ~ 1 -min time scale, the wave normal analysis remains the same as before, and the slow time variations are attributed to the varying source intensity (propagation effects, being linear, remain the same).

2. In the second interpretation, the net power emitted by the source is assumed to remain constant. The slow time variation is then attributable to the statistics of the FDF. Here we assume that our choice of $\Delta t \sim 1$ min is good, but that the assumption of total lack of mutual coherence between the phases of individual plane waves (equation (19)) is incorrect. Instead of this assumption, if we have

$$\langle E_0(\mathbf{u}, \omega) E_0^*(\mathbf{u}', \omega') \rangle = \langle |E_0(\mathbf{u}, \omega) E_0^*(\mathbf{u}', \omega')| \rangle \delta(\mathbf{u} - \mathbf{u}') \cdot \frac{1}{\Delta\omega\sqrt{\pi}} \exp \left[- \left(\frac{\omega - \omega'}{\Delta\omega} \right)^2 \right] \quad (27)$$

then, as shown below, it is possible to account for slow fading. Physically this assumption means that plane waves whose frequencies lie within $\Delta\omega$ of each other are phase correlated. In this sense, $\Delta\omega$ can be viewed as the “coherence bandwidth” of hiss. Note that as expected, equation (27) reduces to equation (19) when $\Delta\omega = 0$.

Then, as seen from equations (18) and (27), a slow time variation of the envelope would result. The time scale and the amplitude of this variation can be experimentally measured, thus providing a method for measuring $\Delta\omega$. From the measured slow variation (~ 30 s) we estimate $\Delta\omega \sim 0.2$ rad/s. Note here that this estimate gives a lower limit on the coherence bandwidth of the hiss source, since any propagation effects could only increase the randomness of the phases of different plane waves that constitute the FDF. Also, it is possible to envision a model in which the phase correlation is due to the angular separation between two waves of the same frequency but different wave normal angles. Further elaboration of the statistical nature of hiss is the subject of a future paper.

4. WAVE NORMAL ANALYSIS

In this section, we present results of analysis of the wave normal direction of hiss during the ~ 3 -hour-long period as shown in Figure 1 and Plate 1. The wave normal measurements were made using electric and magnetic field data at ~ 10 -min intervals. At some of these times only one of the components (electric or magnetic) was available for wave normal determination. Table 1 gives the times and trajectory parameters at which the wave normal analyses were performed. Table 2 gives the relevant satellite attitude and medium parameters. Table 3 gives the measured fading parameters. The measured spin fading in decibels is related to the depth of fading parameter, M , by the following relation:

$$\text{Fading(dB)} = 10 \log \left[\frac{(1+M)}{(1-M)} \right] \quad (28)$$

TABLE 2. Satellite Attitude and Medium Parameters

Time, UT	θ_a , deg	t_{ref} , s	n_e , el/cm ³	B_0 , G	$\Omega = f/f_H$ ($f=1500$ Hz)
0243	93.12 ± 0.01	0.64 ± 0.05	55 ± 1	0.0218 ± 0.0001	0.025
0248	92.95 ± 0.01	1.58 ± 0.05	60 ± 1	0.0181 ± 0.0001	0.030
0253	92.75 ± 0.01	2.52 ± 0.05	55 ± 1	0.0152 ± 0.0001	0.036
0304	92.24 ± 0.01	2.16 ± 0.05	60 ± 1	0.0109 ± 0.0001	0.049
0324	91.09 ± 0.01	2.93 ± 0.05	51 ± 1	0.00679 ± 0.0001	0.079
0334	90.43 ± 0.01	1.80 ± 0.05	45 ± 1	0.00564 ± 0.0001	0.095
0348	89.43 ± 0.01	0.83 ± 0.05	39 ± 1	0.00456 ± 0.0001	0.117
0357	88.75 ± 0.01	1.95 ± 0.05	31 ± 1	0.00408 ± 0.0001	0.131
0409	87.85 ± 0.01	2.42 ± 0.05	31 ± 1	0.00363 ± 0.0001	0.159
0420	87.03 ± 0.01	2.09 ± 0.05	41 ± 1	0.00335 ± 0.0001	0.160
0424	86.74 ± 0.01	2.25 ± 0.05	41 ± 1	0.00327 ± 0.0001	0.164
0428	86.46 ± 0.01	2.41 ± 0.05	32 ± 1	0.00320 ± 0.0001	0.167
0432	86.18 ± 0.01	2.57 ± 0.05	27 ± 1	0.00315 ± 0.0001	0.170
0436	85.91 ± 0.01	2.73 ± 0.05	27 ± 1	0.00311 ± 0.0001	0.172
0438	85.78 ± 0.01	1.29 ± 0.05	27 ± 1	0.00309 ± 0.0001	0.173
0440	85.65 ± 0.01	2.89 ± 0.05	27 ± 1	0.00308 ± 0.0001	0.174
0442	85.52 ± 0.01	1.45 ± 0.05	27 ± 1	0.00306 ± 0.0001	0.175
0450	85.03 ± 0.01	1.77 ± 0.05	24 ± 1	0.00303 ± 0.0001	0.177
0500	84.49 ± 0.01	0.66 ± 0.05	20 ± 1	0.00304 ± 0.0001	0.176
0510	84.00 ± 0.01	2.59 ± 0.05	18 ± 1	0.00310 ± 0.0001	0.173
0528	83.31 ± 0.01	1.81 ± 0.05	20 ± 1	0.00332 ± 0.0001	0.161
0539	82.98 ± 0.01	1.51 ± 0.05	17 ± 1	0.00355 ± 0.0001	0.153

When an integrator with time constant ΔT is used to smooth the data, the apparent depth of fading M_{apparent} is slightly less than the actual depth of fading M_{actual} . These two are related as follows:

$$M_{\text{actual}} = \frac{2\omega_s \Delta T}{\sin(2\omega_s \Delta T)} M_{\text{apparent}} \quad (29)$$

Average wave normals were estimated separately from electric and magnetic measurements. Figure 8 illustrates how wave normal analysis is performed graphically. In this

figure, θ is represented radially, and ϕ azimuthally. For each of the four fading parameters (M^e , M^m , α^e , α^m) we have two measured values. For example, for M^e we have $\overline{M^e} + \Delta M^e$ and $\overline{M^e} - \Delta M^e$. Each of these values corresponds to contour(s) in the (θ, ϕ) plane on which the first equation in (24a) is satisfied. In general each solution leads to two contours as shown in Figure 8. This happens because the whistler mode relations are symmetrical in azimuth in Figure 6. The intersection of constant M^e contours with

TABLE 3. Measured Fading Parameters

Time, UT	M_e , dB	α_e , deg	M_m , dB	α_m , deg	T_{slow} , s
0243	14.7 ± 1.5	142 ± 36	x	x	*
0248	13.1 ± 1.5	135 ± 36	< 1.24	†	*
0253	15.1 ± 1.0	135 ± 36	5.9 ± 1.0	-142 ± 36	~ 36.5
0304	x	x	3.8 ± 1.0	158 ± 36	*
0324	x	x	5.8 ± 1.0	-169 ± 36	~ 56
0334	x	x	3.3 ± 1.0	180 ± 36	*
0348	13.0 ± 1.0	123 ± 36	3.8 ± 1.0	164 ± 36	~ 24
0357	12.6 ± 1.0	130 ± 36	4.9 ± 1.0	-174 ± 36	~ 30
0409	13.8 ± 1.0	106 ± 36	2.4 ± 1.0	-114 ± 36	~ 30
0420	11.3 ± 1.0	130 ± 36	2.5 ± 1.0	-169 ± 36	~ 30
0424	9.8 ± 1.5	143 ± 36	3.5 ± 1.0	124 ± 36	*
0428	7.0 ± 1.0	152 ± 36	< 1.9	†	*
0432	8.2 ± 1.0	143 ± 36	< 1.5	†	~ 30
0436	6.2 ± 1.0	171 ± 36	< 1.8	†	*
0438	4.1 ± 1.0	136 ± 36	< 1.4	†	*
0440	8.9 ± 1.0	-175 ± 36	4.1 ± 1.0	169 ± 36	*
0442	9.9 ± 1.0	157 ± 36	x	x	~ 45
0450	8.0 ± 1.0	124 ± 36	x	x	*
0500	6.3 ± 1.0	155 ± 36	< 1.4	†	*
0510	5.5 ± 1.0	162 ± 36	< 0.9	†	*
0528	5.4 ± 1.0	130 ± 36	x	x	*
0539	7.6 ± 1.0	120 ± 36	x	x	*

x indicates that the corresponding data were not available.

* indicates that no significant slow time fading was observed.

† indicates that the corresponding measurement could not be performed.

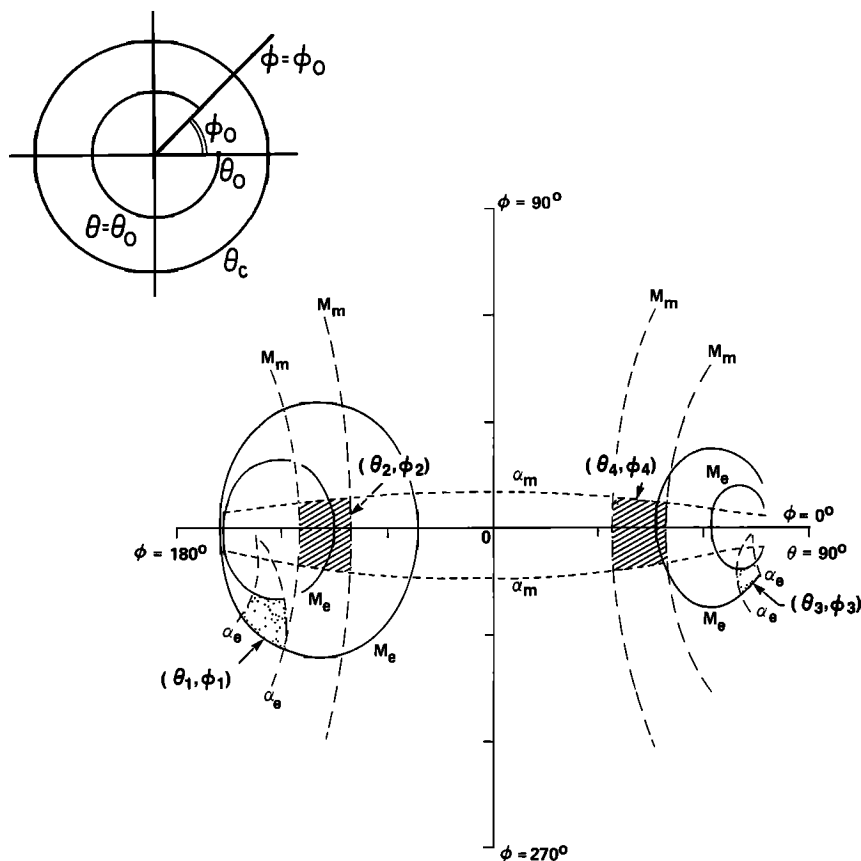


Fig. 8. Fading contours representing a graphical solution to equations (24a) and (24b). Electric field data lead to two solutions shown by stippled region, and magnetic field data lead to two solutions shown by hatched area.

constant α^e contours leads to a region (stippled portion in Figure 8) in the (θ, ϕ) plane which is the average wave normal direction deduced from the electric field fading measurements. Similarly, the magnetic field fading measurements lead to an average wave normal measurement (the hatched region in Figure 8) which in general, for the reason mentioned earlier, is different from the one deduced from the electric field data. Together, these two wave normal measurements represent—in a certain sense—the spread of wave normal directions in the (θ, ϕ) plane. In short, Figure 8 is a graphical solution to equations (24a) and (24b).

The results of the wave normal calculations are given in Table 4. In general we obtain two possible values of wave normal direction from the electric field data and two from the magnetic field data. These are labeled (θ_1, ϕ_1) , and so on. In Table 4, the angle ϕ is the angle that the plane of the wave normal vector and \mathbf{B}_0 makes with the xz plane of Figure 6.

Figure 9 shows (θ_1, θ_2) and (ϕ_1, ϕ_2) as a function of satellite location and time. Figure 10 shows (θ_3, θ_4) and (ϕ_3, ϕ_4) . It is convenient to represent the azimuthal angle with respect to the local magnetic meridional plane, since it allows comparison of the data with ray tracing simulations. Thus in Figures 9 and 10 we plot the wave normal direction (θ, ϕ) such that θ is the angle that the wave normal vector makes with the local magnetic field, and ϕ is the angle that the plane of the wave normal vector and \mathbf{B}_0 makes with the local meridional plane. In Figures 9 and 10, $\phi = 0^\circ$ corresponds to the wave normal angle in the magnetic meridional plane,

with the wave normal pointing toward higher L shells. The angles θ_r and θ_g shown in Figures 9 and 10 are local resonance cone and Gendrin angles, respectively [Gendrin, 1961] (θ_r , the local resonance cone angle [Stix, 1962], is given by $\theta_r = \cos^{-1}(f/f_H)$, whereas $\theta_g = \cos^{-1}(2f/f_H)$ is known as the Gendrin angle [Gendrin, 1961] and is the angle for which $d(\mu \cos \theta)/d\theta = 0$, where μ is the refractive index; for a whistler mode with $f < f_H/2$, the ray direction is along the static magnetic field). The reason we have two solutions is, as mentioned before, that for a spin axis nearly perpendicular to the geomagnetic field, (θ, ϕ) and $(\theta, \pi - \phi)$ are both solutions. Figures 9 and 10 represent these. In addition it is equally possible that these figures represent waves propagating in exactly opposite directions since $(\pi - \theta, \pi + \phi)$ is also a possible solution. With these remarks in mind, the general observations from Figures 9 and 10 can be summarized as follows:

1. All wave normal directions observed over a 3-hour-long period lie within $\pm 45^\circ$ of the $\phi = \pm 90^\circ$ plane. This plane is normal to the local magnetic meridional plane.
2. Near the geomagnetic equator (within $\sim \pm 3^\circ$ latitude) we observe a wave normal angle of $60^\circ \pm 5^\circ$.
3. Away from the equator, wave normal directions are spread out between 30° and 80° .
4. Within experimental accuracy, the wave normal directions are generally less than the Gendrin angle, θ_g .
5. During the entire trajectory not a single wave normal was measured with $\theta \sim 0^\circ$.

Fading patterns in the frequency range $1400 \text{ Hz} < f_c <$

TABLE 4. Results of the Wave Normal Analysis

Time, UT	θ_1 , deg <i>E</i>	ϕ_1 , deg <i>E</i>	θ_2 , deg <i>B</i>	ϕ_2 , deg <i>B</i>	θ_3 , deg <i>E</i>	ϕ_3 , deg <i>E</i>	θ_4 , deg <i>B</i>	ϕ_4 , deg <i>B</i>
0243	82 ± 0.5	174 ± 1.5	x	x	78 ± 8	-13 ± 7	x	x
0248	84 ± 0.5	178 ± 2	> 58	180 ± 30	80 ± 5	-11 ± 4	> 65	0 ± 30
0253	82 ± 1	180 ± 2	37 ± 6	-150 ± 15	80 ± 5	-14 ± 7	38 ± 9	-27 ± 17
0304	x	x	40 ± 5	168 ± 12	x	x	43 ± 4	14 ± 14
0324	x	x	31 ± 5	-170 ± 24	x	x	34 ± 5	-9 ± 21
0334	x	x	44 ± 3	180 ± 15	x	x	44 ± 3	0 ± 15
0348	75 ± 5	-167 ± 5	43 ± 4	170 ± 18	76 ± 3	-12 ± 4	42 ± 5	11 ± 14
0357	70 ± 7	-163 ± 5	37 ± 5	-176 ± 20	73 ± 5	-12 ± 4	35 ± 5	-5 ± 20
0409	75 ± 3	-165 ± 5	60 ± 8	-155 ± 10	77 ± 3	-9 ± 3	55 ± 8	-26 ± 12
0420	64 ± 8	-160 ± 5	39 ± 3	-176 ± 14	71 ± 5	-11 ± 3	36 ± 5	-5 ± 15
0424	56 ± 12	-172 ± 6	52 ± 5	155 ± 10	70 ± 3	-4 ± 3	46 ± 6	35 ± 10
0428	59 ± 8	-172 ± 6	> 57	180 ± 25	69 ± 4	-4 ± 2	58 ± 9	0 ± 30
0432	57 ± 9	-165 ± 5	> 61	180 ± 25	70 ± 3	-7 ± 3	60 ± 7	0 ± 30
0436	58 ± 2	-178 ± 8	> 60	180 ± 20	68 ± 1.5	-2 ± 4	59 ± 7	0 ± 25
0438	62 ± 1.5	-173 ± 2	> 62	180 ± 15	71 ± 2	-2 ± 1	61 ± 7	0 ± 25
0440	52 ± 3	-176 ± 19	52 ± 3	172 ± 14	65 ± 2	3 ± 5	35 ± 4	7 ± 18
0442	51 ± 11	-171 ± 13	x	x	68 ± 4	-4 ± 5	x	x
0450	47 ± 4	-178 ± 18	x	x	66 ± 1.5	0 ± 6	x	x
0500	53 ± 4	-170 ± 5	> 65	180 ± 25	71 ± 1.5	-3 ± 2	60 ± 7	0 ± 30
0510	54 ± 2	-171 ± 5	> 71	180 ± 15	73 ± 1.5	-4 ± 2	> 66	0 ± 25
0528	54 ± 2	-173 ± 5	x	x	73 ± 1.5	-1 ± 2	x	x
0539	65 ± 3	-166 ± 2	x	x	78 ± 1.5	-2 ± 2	x	x

x indicates that the corresponding data were not available.

1900 Hz have the same characteristics as when $f_c = 1500$ Hz, where f_c is the center frequency of the 300-Hz hiss band used for wave normal analysis. Therefore we conclude that over the indicated range the wave normal distributions were more or less the same as those mentioned above.

The results of the wave normal analysis can be understood qualitatively with the help of simple geometric interpretation. Note the following points:

1. The spin axis of the DE 1 satellite is nearly normal to the geomagnetic meridional plane i.e., $\mathbf{a} \perp \mathbf{B}_0$. Thus in Figure 6, $\theta_a \sim 90^\circ$, and yz is the spin plane as well as being the magnetic meridional plane.
2. For the parameters of our case, the whistler mode magnetic field polarization is nearly circular, and the magnetic field is confined to the plane normal to the wave normal vector \mathbf{k} .
3. The electric field polarization has two components: one circular and perpendicular to \mathbf{k} and other parallel to \mathbf{k} . The parallel component dominates at large wave normal angles.
4. Fading patterns are a measure of the projection of the wave electric and magnetic polarization ellipses onto the spin plane (yz).

A wave propagating at a large wave normal angle in the xz (Figure 6) plane would have nearly circular polarization in the spin plane (yz) for its magnetic field, thus leading to only small fading, and the electric field would have a linear polarization, leading to larger fading. This also explains why when dealing with a spread of wave normal angles, the average wave normal angle deduced from the magnetic field fading pattern would be smaller than that deduced from the electric field fading.

The high values of wave normal angles and a spread in the wave normal directions are, in general, consistent with the wave normal analysis of Lefeuvre and coworkers of the ISEE

1 and GEOS 1 data as also discussed in the next section. We note, however, that observations 1, 2 and 5 listed above are special to our data. Also the analysis presented here is the first one where hiss is considered as an enduring phenomenon over a relatively long satellite trajectory over a wide latitude range. As a result of this, we are able to elucidate the source location and nature of hiss as discussed below.

5. INTERPRETATION

In this section we present an interpretation of the measurements in terms of location and nature of the hiss source and also discuss our observations in the light of previous work on the theories of generation and propagation of hiss in the magnetosphere.

5.1. Comments on Analysis Method

The analysis of hiss presented in this paper is based on a new formulation developed to analyze electromagnetic field data received on a satellite [Sonwalkar, 1986]. A few points deserve further attention.

First, consider the role of spin of the satellite, which allows sampling of the wave electric and magnetic polarizations in the spin plane with the help of single electric and magnetic antennae. With two electric and two magnetic field antennae the same purpose could be achieved even if the satellite were not spinning. The important physical result from our study is that over several spin periods the time-averaged wave polarization remains constant. This implies that averaging the polarizations over a few seconds provides increased reliability of estimates of the wave normal direction(s) of hiss.

Second, consider the role of center frequency f_c and the bandwidth Δf chosen for analysis. It is found that larger Δf leads to better-defined spin fades. This permits calculation of fading parameters with more accuracy at the expense

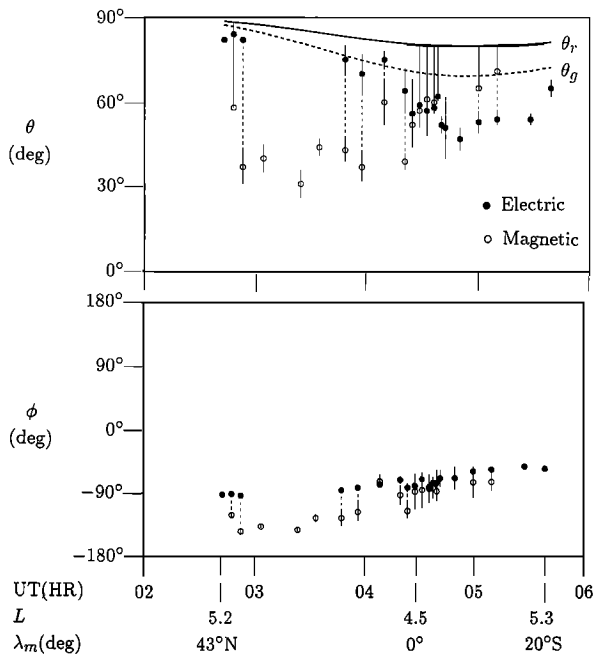


Fig. 9. One of the two possible wave normal distributions (as a function of satellite location) derived from the wave normal analysis. The upper panel shows the wave normal angle with respect to local geomagnetic field. In general we have two angles: one deduced from the electric field and other from the magnetic field data. The dashed line joining these two indicates that these measurements represent a distribution of wave normals in that range. The lower panel shows the distribution in azimuth corresponding to wave normal directions shown in the upper panel. The plane $\phi = 0^\circ$ is the local meridional plane with wave normal pointing toward higher L shells. The angles θ_r and θ_g are the local resonance cone [Stiz, 1962] and the Gendrin angles [Gendrin, 1961], respectively.

of loss in frequency resolution. It appears that the choice of Δf should be decided iteratively after working with the actual data. One possibility would be to take Δf such that the power spectrum in this interval is constant. The data presented in this paper suggest that Δf of a few hundred hertz is a good choice.

Variation of f_c would give properties of hiss in different frequency bands which are needed for a complete picture. In our data we found that the wave normal directions of the hiss in the band 1400 Hz to 1900 Hz were in general the same as those given for $f_c=1500$ Hz.

In this paper we have briefly touched on the subject of the statistical characterization of hiss. Further elaboration of this topic will be the subject of a future paper. Note that looking at the envelope of the signal is only one of several ways of processing data [Sonwalkar, 1986].

5.2. Source Location and Nature

The wave normal analysis carried out in the last section can be used to learn about source location. To this end we draw upon the work of past authors [Muzzio and Angerami, 1972; Thorne et al., 1979; Huang et al., 1983; Lyons and Williams, 1984; Cairo and Lefeuvre, 1986]. The general conclusions of these authors relevant to our study can be summarized as follows:

1. Both Huang et al. [1983] and Thorne et al. [1983] conclude, from their detailed calculation of ray path integrated gain of rays injected at the equator, that local generation (from the thermal noise) of hiss is not consistent with the observed intensity level of hiss. Therefore they propose the existence of a strong embryonic source that generates hiss which is subsequently carried to other regions of the magnetosphere.

2. For cyclotron resonance the gain is maximum at the equator just inside the plasmopause for waves propagating parallel to the Earth's magnetic field [Lyons and Williams, 1984]. Therefore the equator, parallel propagation, and $L \sim 4$ are the favored conditions for an embryonic source. We also note here that Muzzio and Angerami [1972] showed that the upper cutoff of hiss was equatorially controlled.

3. A recent study by Cairo and Lefeuvre [1986] has demonstrated the necessity and usefulness of three dimensional ray tracing simulations to interpret wave normal data on hiss. In particular they have shown that two-dimensional ray tracing is reliable only when waves propagate with small wave normal angle with respect to the Earth's magnetic field in the meridional plane. Since we have measured wave normal angles which are large and in a plane normal to the meridional plane, three-dimensional ray tracing analysis is essential. In what follows we draw heavily on the ray tracing results of the above study. However, we note that the results of the above study are valid for a smooth magnetosphere and do not account for a relatively sharp plasmopause boundary. In our case the satellite was outside but near the plasmopause boundary over the entire 3-hour-long trajectory, and therefore the following analysis may require significant revision.

Let us assume that on September 23, 1983, at the time of our measurement the source of hiss was located on the equator and close to the plasmopause. With the plasma-

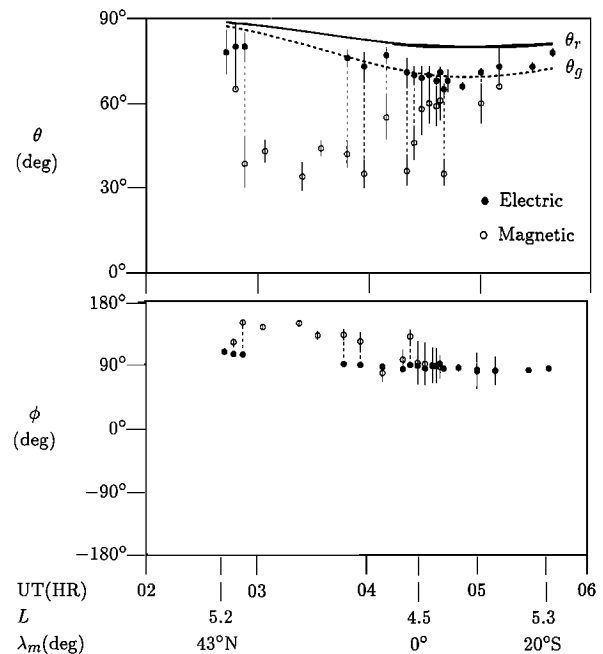


Fig. 10. A second possible set of wave normal distribution that is equally consistent with the September 23, 1983 hiss data. The format is identical to that of Figure 9.

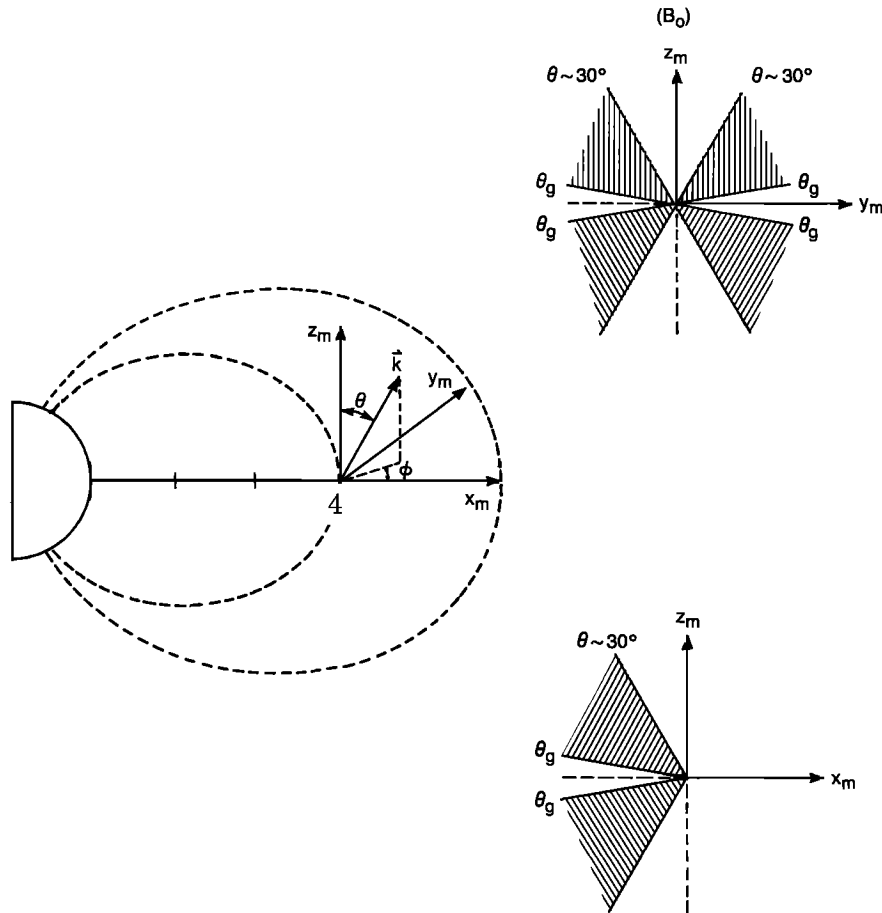


Fig. 11. Schematic representing the radiation characteristics of a possible hiss source. To be consistent with the wave normal distributions shown in Figures 9 and 10, a source at the magnetic equator would radiate with initial wave normal angles in the range $30^\circ < \theta_0 < \theta_g$ and $90^\circ < \phi_0 < 270^\circ$.

pause on this day at $L \sim 4$ this puts the source location at $L \sim 4$, $\lambda_m = 0^\circ$. Let (θ_0, ϕ_0) denote the initial wave normal direction at the source, where θ_0 is the wave normal angle with respect to the geomagnetic field and ϕ_0 is the azimuthal angle; $\phi = 0^\circ$ corresponds to a wave normal in the magnetic meridional plane, pointing toward higher L shells. Assuming that rays propagate directly from the source to the observation point, we ask, What kind of radiation from such a source would yield the wave normal distribution observed on the DE 1 satellite? What range of initial wave normal distribution would lead to the observed wave normal directions shown in Figures 9 and 10?

To investigate this question, we make use of the following results of *Cairo and Lefeuvre* [1986]: (1) Rays with starting wave normals in the range $0^\circ < \theta_0 < \theta_g$ propagate toward higher L shells. Waves in the range $\theta_g < \theta_0 < \theta_r$ propagate toward lower L shells. (2) Waves with wave normal angles close to $\theta_0 \sim 0^\circ$ very quickly, within a 10° – 15° latitude range, align themselves in the magnetic meridional plane with wave normal pointing outward ($\phi = 0^\circ$). (3) Wave normals with $\phi_0 \sim 0^\circ$ remain in the same plane, i.e., $\phi = 0^\circ$. (4) Wave normal directions eventually become large with respect to the Earth's magnetic field.

Our conclusion based on wave normal analysis and on the ray tracing study of *Cairo and Lefeuvre* [1986] is that a

source at the equator emitting at $\theta \sim 0^\circ$ is not consistent with the observed wave normal characteristic of hiss along the September 23, 1983, DE 1 trajectory. Similarly, a source emitting with initial wave normals in the meridional plane pointing outward is also not consistent with our data. These two conclusions are based on points 2 and 3 mentioned above and the fact that our measured wave normal angles always lie in the plane normal to the meridional plane.

A more consistent source appears to be one located close to the plasmapause, emitting rays with wave normals in a range $30^\circ < \theta_0 < \theta_g$ and $90^\circ < \phi_0 < 270^\circ$. Figure 11 gives a schematic of such a source near the equator. This source is consistent with the observed wave normal distribution (section 4), except that it does not quite explain the lack of spread in the wave normal distribution observed close to the equator. We note that the absence of any wave normal angles $\theta \sim 0^\circ$ in our data is indicative of a generation condition in which at plane $\phi_0 \sim 180^\circ$, the wave normal angle θ_0 is closely confined to the vicinity of the Gendrin angle, i.e., $\theta_0 \sim \theta_g$. In such a case, according to the ray tracing results of *Cairo and Lefeuvre* [1986], θ for rays spreading out from the source region would not reach $\theta \sim 0^\circ$ until they reach very high ($> 45^\circ$) latitudes. However, if the spread of initial wave normals θ_0 in the $\phi_0 \sim 180^\circ$ plane is large, then $\theta \sim 0^\circ$ would be observable at lower latitudes. Such

a circumstance may explain occasional previous measurements of $\theta \sim 0^\circ$ for hiss [Lefeuvre *et al.*, 1983; Lefeuvre and Helliwell, 1985; Hayakawa *et al.*, 1986].

On this particular day the satellite was near the plasmasphere boundary, and a detailed ray tracing may be required which takes into account the actual cold plasma distribution on this day. Another point to note is that we have not considered the possibility of an off-equatorial source; auroral hiss, for example, has been suggested as a possible source for plasmaspheric hiss [Huang *et al.*, 1983]. To get a more complete understanding of the source region we must find the wave normal distributions inside and outside the plasmopause.

5.3 Discussion

The inference of high wave normal angles at the source region is important in its implications for various proposed mechanisms for these emissions. In particular, those mechanisms that require field-aligned propagation near the source region [Thorne *et al.*, 1973] would have to be revised or extended in view of these results. An interesting point to note is that a whistler mode wave with wave normal direction close to the local Gendrin angle θ_g has ray direction parallel to the local geomagnetic field. Thus a wave packet with the wave normal direction $\theta \sim \theta_g$ would interact with the energetic electrons (which travel along the geomagnetic field) for a relatively long period, leading to an interaction length comparable to the case when the wave normal is aligned with the geomagnetic field.

Two slow time variations were observed in our hiss data. One is over a time scale of ~ 30 s and is interpreted as either a varying source intensity or the result of the finite coherence bandwidth of the hiss source. To decide between these two alternatives, further work is needed. In particular it will be useful to see if particle data show time variations on the same time scale; another line of attack would be to check other consequences of assuming a finite coherence bandwidth and to test them against data. The time variation over a ~ 10 - to 15-min scale could be due to spatial or temporal variation, and we are not at this time able to provide an explanation to account for this fading. However, we note that Parady *et al.* [1975] also noticed fading on this time scale.

The implied coherence bandwidth of hiss is also important, since it may mean that the generation mechanisms of hiss and more structured noises such as spontaneous chorus emissions are inherently similar. In this connection, we refer to Koons [1981], who has considered the role of hiss in magnetospheric chorus emissions. Recently, Helliwell *et al.* [1986] have shown that a simulated band-limited random noise can trigger choruslike discrete emissions.

6. SUMMARY AND CONCLUSIONS

A detailed study of VLF/ELF hiss as a spatially and temporally enduring phenomenon has revealed new relationships among the properties of hiss observed in different regions of the magnetosphere. We have analyzed hiss signals received by electric and magnetic field antennae aboard the DE 1 satellite along a ~ 3 -hour-long trajectory. On September 23, 1983, a hiss band (< 2 kHz) was observed continuously during the 0236–0539 UT period, over a range of geomagnetic latitudes from $\lambda_m = 45^\circ\text{N}$ to $\lambda_m = 20^\circ\text{S}$, and L shells of $L = 4.3$ to $L = 5.3$. Electron density deduced from

in situ measurements of upper hybrid resonance emissions and remote measurements based on the whistler method indicate that during this time the DE 1 satellite was outside but near the boundary of the plasmasphere. Our observations can be summarized as follows: (1) The general character of the electric and magnetic field spectrum remained the same throughout the 3-hour-long period, exhibiting an intensity peak at 1550 Hz. (2) The intensities of both the electric and the magnetic field decreased by ~ 30 dB during this interval. (3) Well-defined fading patterns at twice the spin period (3.04 s) were observed throughout this period. These patterns were stable over a time scale of ~ 1 min. (4) A slower fading pattern with a time scale of 30 s and superimposed on the spin fading was observed approximately 30% of the time. (5) The hiss intensity also showed fading over a time scale of ~ 10 –15 min.

Application of the FDF technique to the interpretation of spin fading patterns led to the measurement of wave propagation direction(s). The results can be summarized as follows: (1) Near the geomagnetic equator (within $\sim \pm 3^\circ$ latitude) we observed a wave normal angle of $60^\circ \pm 5^\circ$ with respect to the local geomagnetic field. (2) Away from the equator, wave normal directions were distributed in a range from 30° to 80° with respect to the local geomagnetic field. (3) All wave normal directions observed over a 3-hour-long period were within $\sim \pm 45^\circ$ of the plane normal to the local magnetic meridian.

By combining wave normal measurements with results from the three dimensional ray tracing simulations of Cairo and Lefeuvre [1986], we conclude that the data were consistent with a source at the magnetic equator, radiating with initial wave normal angles in the range $30^\circ < \theta_0 < \theta_g$ and $90^\circ < \phi_0 < 270^\circ$, where θ_g is the local Gendrin angle [Gendrin, 1961]. The FDF formulation has also permitted elucidation of the statistical nature of hiss. The slow fading (~ 30 s) is interpreted in terms of a coherence bandwidth $\Delta\omega$ of about 0.2 rad/s.

The inference of high wave normal angles at the source region is important in its implications for various proposed mechanisms for these emissions. In particular, those mechanisms that require field-aligned propagation near the source region [Thorne *et al.*, 1973] may have to be revised or extended in view of these results. The implied coherence of hiss is also important, since it may mean that the generation mechanisms of spontaneous chorus emissions and hiss are inherently similar [Koons, 1981; Helliwell *et al.*, 1986].

APPENDIX: RELATIONS BETWEEN FDF, FOURIER, AND WDF REPRESENTATIONS

In this appendix we provide a formal connection between FDF, WDF, and Fourier representations of a signal propagating in a single mode in a magnetoplasma. A more detailed discussion can be found in the work by Sonwalkar [1986].

A1. Relation Between FDF and Fourier Representations

An arbitrary electromagnetic field present in some region of space $\Delta\mathbf{r}$ centered around \mathbf{r}_0 during a time interval Δt centered around t_0 can be decomposed into its Fourier transform (equation (1), section 3.1). Furthermore, if the signal is propagating in a single mode, we have $\omega = \omega(\mathbf{k})$, and the Fourier transform can be written as [Bekefi, 1966]

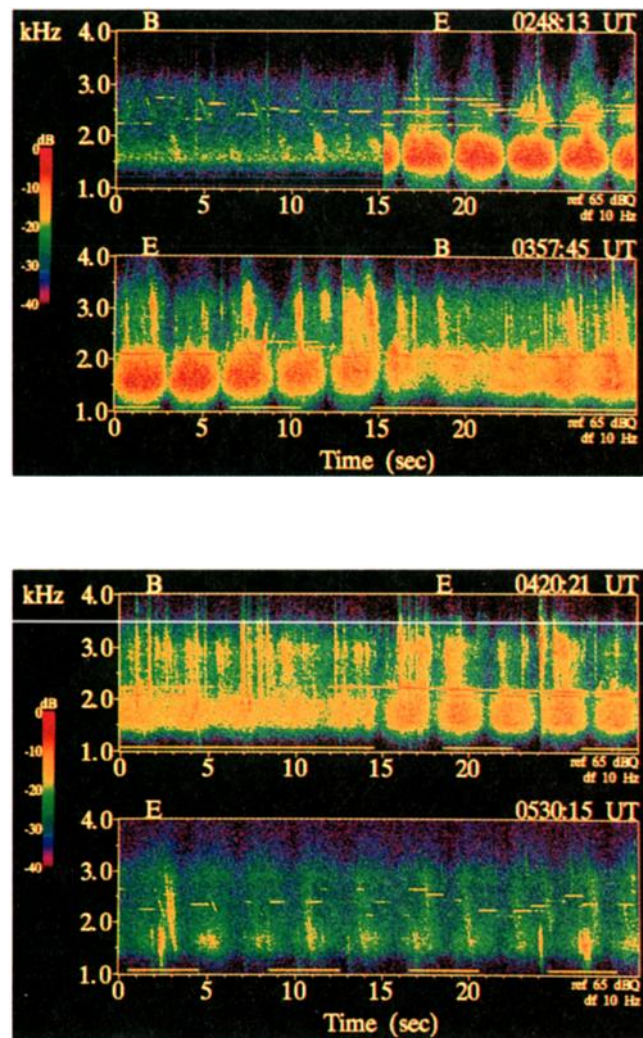


Plate 1. Typical hiss spectra around four regions indicated in Figure 1. The constant frequency pulses seen in the spectra are Siple transmitter signals. The spin fading patterns lead to the measurement of wave normal direction(s) of hiss.

$$\mathbf{E}(\mathbf{r}, t) = \int_{\mathbf{k}} \mathbf{A}_{\mathbf{k}}^e(\mathbf{k}) e^{[i(\omega(\mathbf{k})t - \mathbf{k} \cdot \mathbf{r})]} d\mathbf{k} \quad (\text{A1})$$

where $\mathbf{A}_{\mathbf{k}}^e(\mathbf{k})d\mathbf{k}$ is the electric field amplitude of the plane wave propagating with frequency $\omega(\mathbf{k})$ and wave normal vector \mathbf{k} .

In a magnetoplasma with \mathbf{B}_0 as the axis of symmetry, it is preferable to have (θ, ϕ, ω) as the independent variables. As pointed out by Storey and Lefeuvre [1974], another reason for using (θ, ϕ, ω) as independent variables, instead of \mathbf{k} , is that for an extraordinary mode propagating in a magnetoplasma, $\omega(\mathbf{k})$ is ambiguous, i.e., for a given $|\mathbf{k}|$ there are two possible values of ω , whereas given ω , $|\mathbf{k}|$ is always uniquely defined for a given (θ, ϕ) . The third reason for this change of variables, when representing an unknown signal, is to take advantage of the fact that both \mathbf{R}^e and \mathbf{k} are known functions of (θ, ϕ, ω) . Thus, if $\mathbf{A}^e(\theta, \phi, \omega)d\theta d\phi d\omega$ represents the amplitude of the plane wave of frequency ω , propagating in the direction (θ, ϕ) , then

$$\mathbf{A}^e(\theta, \phi, \omega) = J \mathbf{A}_{\mathbf{k}}^e(\mathbf{k}) \quad (\text{A2})$$

J is the Jacobian for the transformation:

$$J = \frac{\partial(k_x, k_y, k_z)}{\partial(\theta, \phi, \omega)} = V_g^{-1} k^2 \sin \theta \quad (\text{A3})$$

where $k = |\mathbf{k}|$ and $V_g = |\partial\omega/\partial\mathbf{k}|$ are the moduli of the wave vector and the group velocity, respectively. Because of the $\sin \theta$ term in (A3), the function $\mathbf{A}^e(\theta, \phi, \omega)$ vanishes at $\theta = 0$. Therefore it is desirable to use the variable $\cos \theta$ instead of θ to avoid this difficulty. Since the polarization \mathbf{R}^e of a wave propagating in a given mode is a known function of (θ, ϕ, ω) , it is convenient to separate the polarization and the intensity part of the amplitude of a plane wave. Thus if $E_0(\theta, \phi, \omega)$ is proportional to the wave amplitude, then the amplitude of the wave with frequency ω and propagating in the direction (θ, ϕ) is $E_0(\theta, \phi, \omega)\mathbf{R}^e(\theta, \phi, \omega)d(\cos \theta)d\phi d\omega$, where

$$E_0(\theta, \phi, \omega)\mathbf{R}^e(\theta, \phi, \omega) = V_g^{-1} k^2 \mathbf{A}_{\mathbf{k}}^e(\mathbf{k}) \quad (\text{A4})$$

The complex function $E_0(\theta, \phi, \omega)$ is called the field distribution function (FDF). Equation (A4) is the formal connection between the FDF and the Fourier transform $\mathbf{A}_{\mathbf{k}}^e(\mathbf{k})$ of an arbitrary signal propagating in a single mode. Note that for a given single mode, each of the quantities \mathbf{R}^e , V_g , k are known functions of (θ, ϕ, ω) . Thus given the FDF, the corresponding Fourier representation is known uniquely and vice versa. Equation (A4) says that the magnitude of the FDF is proportional to the electric field amplitude of the corresponding plane wave and the phase of the FDF is the same as that of the plane wave within an additive constant. The proportionality and the additive constants are known functions of (θ, ϕ, ω) . From equation (4) of section 3 we get for the magnetic field component of an arbitrary wave propagating in a single mode,

$$E_0(\theta, \phi, \omega) \frac{\mathbf{k}(\theta, \phi, \omega) \times \mathbf{R}^e(\theta, \phi, \omega)}{\omega} = V_g^{-1} k^2 \mathbf{A}_{\mathbf{k}}^m(\mathbf{k}) \quad (\text{A5})$$

where $\mathbf{A}_{\mathbf{k}}^m$ is the Fourier transform of the magnetic field $\mathbf{B}(\mathbf{r}, t)$ of the signal propagating in a single mode.

Equations (A1)–(A5) lead to the representation of such signals by equations (2) or (3) and (4) of section 3.1. The major advantage of the FDF representation over the Fourier

representation is that it takes into account all the known dispersion and polarization relationships of the mode in which the wave is propagating. Thus, only one complex scalar function $E_0(\theta, \phi, \omega)$ is sufficient to represent the signals compared to two three dimensional Fourier transforms, namely $\mathbf{A}_{\mathbf{k}}^e$ and $\mathbf{A}_{\mathbf{k}}^m$. It should be noted here that the FDF is specific to a given mode of propagation and, unlike the Fourier representations, the FDF's of signals when more than one mode is present do not simply add. The general expression for fields that consist of a superposition of waves propagating in multiple modes is given by

$$\mathbf{E}(\mathbf{r}, t) = \sum_M \int_{\omega} \int_{\theta} \int_{\phi} E_{0,M}(\theta, \phi, \omega) \mathbf{R}_M^e(\theta, \phi, \omega) \cdot e^{[i(\omega t - \mathbf{k}_M(\theta, \phi, \omega) \cdot \mathbf{r})]} d(\cos \theta) d\phi d\omega \quad (\text{A6})$$

where $E_{0,M}(\theta, \phi, \omega)$ is the FDF for mode M and $\mathbf{R}_M^e(\theta, \phi, \omega)$ and $\mathbf{k}_M(\theta, \phi, \omega)$ are the polarization and wave normal vectors as a function of (θ, ϕ, ω) for mode M . An analogous expression can be written down for the wave magnetic field.

A2. Relation Between FDF and WDF Representations

The FDF representation of signals is completely general and can be used to represent a large variety of signals propagating in a single mode or multiple modes. One such application is the propagation of electromagnetic signals in the Earth's magnetosphere. Additional restrictions may be specified on the given FDF depending on the particular signal under consideration. For example a constant frequency (ω_0) signal from a ground transmitter is appropriately represented by a deterministic FDF which satisfies the following condition:

$$E_0(\theta, \phi, \omega) = E_0(\theta, \phi, \omega_0) \delta(\omega - \omega_0) \quad (\text{A7})$$

An example of a plane wave is given in equation (5), section 3 which is a special case of equation (A7).

The wideband VLF noise known as hiss has a structureless spectrum, and therefore Storey [1971] suggested that this noise be treated as composed of infinitesimally small plane waves propagating without any mutual coherence. In such a formulation, hiss is described by a wave distribution function $F(\mathbf{u}, \omega)$ such that $F(\mathbf{u}, \omega)d\sigma d\omega$ is the ensemble average wave energy density due to waves with angular frequencies in the range from ω to $\omega + d\omega$ and with directions of propagation lying in the element of solid angle $d\sigma$ centered on the direction of unit vector $\mathbf{u}(\theta, \phi)$, where $\mathbf{k} = |\mathbf{k}| \mathbf{u}$ [Storey and Lefeuvre 1979].

In the FDF representation of hiss, we assume that the FDF, $E_0(\theta, \phi, \omega)$ or $E_0(\mathbf{u}, \omega)$, is a complex random variable in (θ, ϕ, ω) and that its various ensemble averages are used to characterize hiss. Generally the ensemble averages that enter into the calculations when we connect the FDF to the received voltages and envelopes of voltages (or time correlations) are $\langle E_0(\theta, \phi, \omega) \rangle$ and $\langle E_0(\theta, \phi, \omega) E_0^*(\theta', \phi', \omega') \rangle$. In general, if we assume that the phases of individual plane waves are uniformly distributed in the interval $(0 - 2\pi)$, the first of the above averages will be zero. The representation of the second averages can be done in many ways, and the clue for this has to come from the experimental data. In

section 3 we presented two models for this term (equations (19) and (27)). However, to relate FDF to WDF, it is necessary to assume that the following relation (same as equation (19)) holds:

$$\langle E_0(\mathbf{u}, \omega) E_0^*(\mathbf{u}', \omega') \rangle = \langle E_0(\mathbf{u}, \omega) E_0^*(\mathbf{u}, \omega) \rangle \delta(\mathbf{u} - \mathbf{u}') \delta(\omega - \omega') \quad (\text{A8})$$

This assumption is equivalent to Storey and Lefeuvre's [1979] assumption about no mutual coherence between individual plane waves. Then the relation between FDF and WDF is given by

$$F(\mathbf{u}, \omega) = \frac{1}{2\mu_0 V_g(\mathbf{u}, \omega)} \langle E_0(\mathbf{u}, \omega) E_0^*(\mathbf{u}, \omega) \rangle \cdot \text{Re} \left[\mathbf{R}^e(\mathbf{u}, \omega) \times \left(\frac{\mathbf{k}(\mathbf{u}, \omega) \times \mathbf{R}^{e*}(\mathbf{u}, \omega)}{\omega} \right) \right] \cdot \mathbf{u} \quad (\text{A9})$$

Re in the above equation denotes the real part of the quantity in the square brackets. In proving (A9) we have used Storey and Lefeuvre's [1980] definition that energy density e is given by

$$e = \frac{1}{2\mu_0 V_g} \text{Re}(\mathbf{E} \times \mathbf{B}^*) \cdot \mathbf{u}$$

where \mathbf{E} and \mathbf{B} are the amplitudes of the elementary plane wave propagating with the wave normal $\mathbf{k}(\theta, \phi, \omega)$.

Equation (A9) is the formal connection between FDF and WDF with the assumption that individual wavelets propagate with no mutual coherence.

It is clear that the WDF representation requires the assumption (A8) in its formulation, whereas in the FDF formulation of hiss one has several possible choices depending on the statistical description of hiss. In fact, at times, the experimental data may demand a choice which is different than equation (A8). An example of this was considered in section 3.6.

Another difference between the WDF and FDF representations is that the WDF is related to the signal energy under the restriction given by equation (A8), whereas the FDF is related to the amplitude and phase of the electric and magnetic field. Typically, satellite wave receivers with electric and magnetic antennae measure fields, not energy, consequently a detailed description of the measurement process is not possible in WDF representations. There are two circumstances where this problem is realized most acutely. One is in the representation of a ground transmitter signal, where the deterministic representation is preferable and the motion of the satellite cannot be ignored. While assumption (A8) can be justified for the definition of the WDF of a ground transmitter signal, one cannot justify the assumption of ergodicity that is necessary to provide a connection between a single measurement and the ensemble averages. On the other hand, a deterministic FDF representation allows for motion of the satellite to be taken into account, and the Doppler shift is used to discriminate multiple paths [Sonwalkar et al., 1984; Sonwalkar, 1986]. The second circumstance concerns the investigation of antenna characteristics. While the WDF representation cannot be used to study the antenna response function, the FDF formulation can be conveniently applied to measure the wave properties

as well as to experimentally determine the antenna response function [Sonwalkar and Inan, 1986; Sonwalkar, 1986].

Acknowledgments. We thank our colleagues in the STAR Laboratory, in particular, R. A. Helliwell, D. L. Carpenter, L. R. O. Storey and T. F. Bell, for many useful comments and discussions. We also thank D. A. Gurnett and A. Persoon of the University of Iowa for providing the cold plasma density data (Figure 2). The spectrograms and amplitude charts were ably produced by J. Yarbrough. This research was supported by National Aeronautics and Space Administration (NASA) under grant NAS5-25744 to Stanford University.

The editor thanks F. Lefeuvre and K. Molvig for their assistance in evaluating this paper.

REFERENCES

- Barrington, R. E., J. S. Belrose, and D. A. Keeley, Very low frequency noise bands observed by the Alouette 1 satellite, *J. Geophys. Res.*, **68**, 6539, 1963.
- Bekefi, G., *Radiation Processes in Plasmas*, John Wiley and Sons, Inc., New York, 377, 1966.
- Cairo, L., and F. Lefeuvre, Localization of sources of ELF/VLF hiss observed in the magnetosphere: Three-dimensional ray tracing, *J. Geophys. Res.*, **91**, 4352, 1986.
- Church, S. R., and R. M. Thorne, On the origin of plasmaspheric hiss: Ray path integrated amplification, *J. Geophys. Res.*, **88**, 7941, 1983.
- Dunckel, N., and R. A. Helliwell, Whistler mode emissions on the OGO 1 satellite, *J. Geophys. Res.*, **74**, 6731, 1969.
- Gendrin, R., Le guidage des whistlers par le champ magnetique, *Planet. Space Sci.*, **5**, 274, 1961.
- Gurnett, D. A., and B. J. O'Brien, High-latitude geophysical studies with satellite INJUN 3, 5, Very-low-frequency electromagnetic radiation, *J. Geophys. Res.*, **69**, 65, 1964.
- Hayakawa, M., M. Parrot, and F. Lefeuvre, The wave normals of ELF hiss emissions observed on board GEOS 1 at the equatorial and off-equatorial regions of the plasmasphere, *J. Geophys. Res.*, **91**, 7989, 1986.
- Helliwell, R. A., *Whistlers and Related Ionospheric Phenomenon*, Stanford University Press, Stanford, Calif., 349, 1965.
- Helliwell, R. A., and J. P. Katsufakis, VLF wave injection experiment into the magnetosphere from Siple station, Antarctica, *J. Geophys. Res.*, **79**, 2511, 1974.
- Helliwell, R. A., D. L. Carpenter, U. S. Inan, and J. P. Katsufakis, Generation of band-limited VLF noise using the Siple transmitter: A model for magnetospheric noise, *J. Geophys. Res.*, **91**, 4381, 1986.
- Huang, C. Y., C. K. Goertz, and R. R. Anderson, A theoretical study of plasmaspheric hiss generation, *J. Geophys. Res.*, **88**, 7927, 1983.
- Imhof, W. L., J. B. Reagan, H. D. Voss, E. E. Gaines, D. W. Datlowe, J. Mobilia, R. A. Helliwell, U. S. Inan, and J. P. Katsufakis, Direct observation of radiation belt electrons precipitated by the controlled injection of VLF signals from a ground-based transmitter, *Geophys. Res. Lett.*, **10**, 361, 1983.
- Inan, U. S., and D. L. Carpenter, Lightning-induced electron precipitation events observed at $L \sim 2.4$ as phase and amplitude perturbations on subionospheric VLF signals, *J. Geophys. Res.*, **92**, 3293, 1987.
- Inan, U. S., D. L. Carpenter, R. A. Helliwell, and J. P. Katsufakis, Subionospheric VLF/LF phase perturbations produced by lightning-whistler induced particle precipitation, *J. Geophys. Res.*, **90**, 7457, 1985.
- Kennel, C. F., and H. E. Petschek, Limit on stably trapped particle fluxes, *J. Geophys. Res.*, **71**, 1, 1966.
- Koons, H. C., The role of hiss in the magnetospheric chorus emissions, *J. Geophys. Res.*, **86**, 6745, 1981.
- Lefeuvre, F., and R. A. Helliwell, Characterization of the sources of VLF hiss and chorus observed on GEOS 1, *J. Geophys. Res.*, **90**, 6419, 1985.
- Lefeuvre, F., M. Parrot, and C. Delannoy, Wave distribution functions estimation of VLF electromagnetic wave observed on board GEOS 1, *J. Geophys. Res.*, **86**, 2359, 1981.
- Lefeuvre, F., M. Parrot, L. R. O. Storey, and R. R. Anderson, Wave distribution functions for plasmaspheric hiss observed on

- board ISEE 1, *Tech. Note LPCE/6*, Lab. de Phys. et Chim. de l'Environ., Orleans, France, 1983.
- Lyons, L. R., and D. J. Williams, *Quantitative Aspects of Magnetospheric Physics*, D. Reidel Publishing Company, Boston, 231, 1984.
- Lyons, L. R., R. M. Thorne, and C. F. Kennel, Pitch angle diffusion of radiation belt electrons within the plasmasphere, *J. Geophys. Res.*, **77**, 3455, 1972.
- Muzzio, J. L. R., and J. Angerami, OGO 4 observations of extremely low frequency hiss, *J. Geophys. Res.*, **77**, 1157, 1972.
- Parady, B. K., D. D. Eberlein, J. A. Marvin, W. W. L. Taylor, and L. J. Cahill, Jr., Plasmaspheric hiss observations in the evening and afternoon quadrants, *J. Geophys. Res.*, **80**, 2183, 1975.
- Parrot, M., and F. Lefeuvre, Statistical study of the propagation characteristics of ELF hiss observed on GEOS-1, inside and outside plasmasphere, *Ann. Geophys., Gauthier Villars*, **5A**, 363, 1986.
- Russell, C. T., R. E. Holzer, and E. J. Smith, OGO 3 Observations of ELF noise in the magnetosphere, 1, Spatial extent and frequency of occurrence, *J. Geophys. Res.*, **74**, 755, 1969.
- Scarf, F. L., D. A. Gurnett, and W. S. Kurth, Measurement of plasma wave spectra in Jupiter's magnetosphere, *J. Geophys. Res.*, **86**, 8181, 1981.
- Scarf, F. L., R. W. Fredricks, and G. M. Crook, Detection of electromagnetic and electrostatic waves on OV3-3, *J. Geophys. Res.*, **73**, 1723, 1968.
- Shawhan, S. D., Estimation of wave vector characteristics, *Adv. Space Res.*, **2**, 31, 1983.
- Shawhan, S. D., D. A. Gurnett, D. L. Odem, R. A. Helliwell, and C. G. Park, The plasma wave and quasi-static electric field instrument (PWI) for Dynamic Explorer-A, *Space Sci. Instrum.*, **5**, 535, 1981.
- Smith, E. J., A. M. A. Frandsen, B. T. Tsurutani, R. M. Thorne, and K. W. Chan, Plasmaspheric hiss intensity variation during magnetic storms, *J. Geophys. Res.*, **79**, 2507, 1974.
- Sonwalkar, V. S., New signal analysis techniques and its application to space physics, Ph.D. thesis, Stanford Univ., Stanford, Calif., 1986.
- Sonwalkar, V. S., and U. S. Inan, Measurements of Siple transmitter signal on the DE-1 satellite: Wave normal direction and antenna effective length, *J. Geophys. Res.*, **91**, 154, 1986.
- Sonwalkar, V. S., T. F. Bell, R. A. Helliwell, and U. S. Inan, Direct multiple path magnetospheric propagation: A fundamental property of the VLF nonducted waves *J. Geophys. Res.*, **89**, 2823, 1984.
- Stix, T. H., *The Theory of Plasma Waves*, McGraw-Hill, New York, 276, 1962.
- Storey, L. R. O., Electric field experiments: alternating fields, in *The ESRO Geostationary Magnetospheric Satellite, SP-60*, p. 267, Eur. Space Res. Organ., Neuilly-sur-Seine, France, 1971.
- Storey, L. R. O., and F. Lefeuvre, Theory for the interpretation of measurements of a random electromagnetic field in space, *Space Res.*, **14**, 381, 1974.
- Storey, L. R. O., and F. Lefeuvre, Analysis of a wave field in a magnetoplasma, II, The integration kernels, *Geophys. J. R. Astron. Soc.*, **62**, 173, 1979.
- Taylor, W. L., and D. A. Gurnett, The morphology of VLF emissions observed with the INJUN 3 satellite, *J. Geophys. Res.*, **73**, 5615, 1968.
- Thorne, R. M., E. J. Smith, R. K. Burton, and R. E. Holzer, Plasmaspheric hiss, *J. Geophys. Res.*, **78**, 1581, 1973.
- Thorne, R. M., S. R. Church, and D. J. Gorney, On the origin of plasmaspheric hiss: The importance of wave propagation and plasmopause, *J. Geophys. Res.*, **84**, 5241, 1979.
- Voss, H. D., W. L. Imhof, J. Mobilia, E. E. Gaines, M. Walt, U. S. Inan, R. A. Helliwell, D. L. Carpenter, J. P. Katsufakis, and H. C. Chang, Lightning induced electron precipitation, *Nature*, **312**, 740, 1984.

U. S. Inan and V. S. Sonwalkar, Stanford University, STAR Laboratory, Department of Electrical Engineering/SEL, Durand 324, Stanford, CA 94305.

(Received June 23, 1987;
revised February 18, 1988;
accepted February 18, 1988.)